Journal of Nanobiotechnology

RESEARCH

Open Access

Bio-orthogonal click chemistry strategy for PD-L1-targeted imaging and pyroptosis-mediated chemo-immunotherapy of triple-negative breast cancer

Yan Wang[1], Yanhong Chen[1], Ding-Kun Ji[3], Yuelin Huang[1], Weixi Huang[1], Xue Dong[1], Defan Yao[1,2*] and Dengbin Wang[1,2*]

Abstract

Background The combination of programmed cell death ligand-1 (PD-L1) immune checkpoint blockade (ICB) and immunogenic cell death (ICD)-inducing chemotherapy has shown promise in cancer immunotherapy. However, triple-negative breast cancer (TNBC) patients undergoing this treatment often face obstacles such as systemic toxicity and low response rates, primarily attributed to the immunosuppressive tumor microenvironment (TME).

Methods and results In this study, PD-L1-targeted theranostic systems were developed utilizing anti-PD-L1 peptide (APP) conjugated with a bio-orthogonal click chemistry group. Initially, TNBC was treated with azide-modified sugar to introduce azide groups onto tumor cell surfaces through metabolic glycoengineering. A PD-L1-targeted probe was developed to evaluate the PD-L1 status of TNBC using magnetic resonance/near-infrared fluorescence imaging. Subsequently, an acidic pH-responsive prodrug was employed to enhance tumor accumulation via bio-orthogonal click chemistry, which enhances PD-L1-targeted ICB, the pH-responsive DOX release and induction of pyroptosis-mediated ICD of TNBC. Combined PD-L1-targeted chemo-immunotherapy effectively reversed the immune-tolerant TME and elicited robust tumor-specific immune responses, resulting in significant inhibition of tumor progression.

Conclusions Our study has successfully engineered a bio-orthogonal multifunctional theranostic system, which employs bio-orthogonal click chemistry in conjunction with a PD-L1 targeting strategy. This innovative approach has been demonstrated to exhibit significant promise for both the targeted imaging and therapeutic intervention of TNBC.

Keywords Click chemistry, Metabolic glycoengineering, Cancer immunotherapy, Prodrug, Triple negative breast cancer

*Correspondence:
Defan Yao
yaodefan@xinhuamed.com.cn
Dengbin Wang
wangdengbin@xinhuamed.com.cn
Full list of author information is available at the end of the article

Graphical abstract

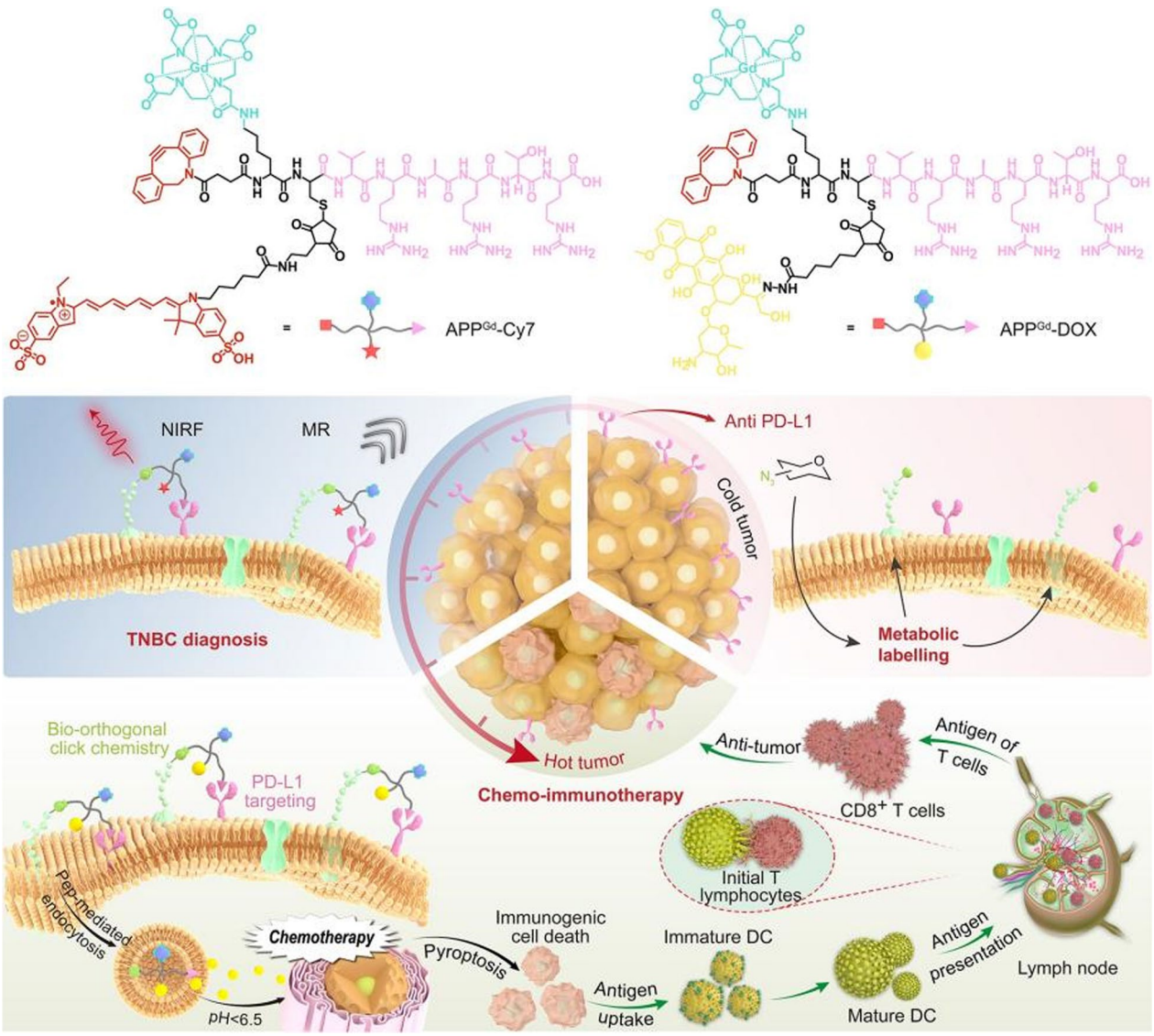

Introduction

Triple-negative breast cancer (TNBC) demonstrates the most aggressive subtype with poorest outcomes and highest propensity for metastasis among all breast cancers [1]. Over the past few years, immune checkpoint blockade (ICB) directed towards programmed cell death protein 1 (PD-1)/programmed death-ligand 1 (PD-L1) have exhibited prolonged survival outcomes in solid tumors [2–6]. A greater prevalence of PD-L1 expression has been observed in TNBC in comparison to other subtypes of breast cancer, indicating that PD-L1 may represent a promising therapeutic target [7, 8]. Nevertheless, the efficacy of ICB monotherapy in TNBC is constrained by a poorly immunogenic tumor microenvironment (TME) and limited tumor penetration [1, 9].

Hence, reversal of immunosuppressive tumor microenvironment (ITM) is crucial to maximizing ICB efficacy in TNBC. Numerous studies have demonstrated that specific chemotherapeutic agents, including doxorubicin (DOX) [10], paclitaxel [11], and oxaliplatin [12], not only elicit antitumor cytotoxic effects but also facilitate immunogenic cell death (ICD). This process involves the release of immunostimulatory danger-associated molecular patterns (DAMPs) such as calreticulin (CRT), high mobility

group box 1 (HMGB1), and adenosine triphosphate (ATP) [13]. DAMPs are essential in promoting dendritic cell (DC) maturation and facilitating antigen presentation to T cells within lymph nodes, ultimately leading to the activation of adaptive immunity [14]. Accumulating evidence indicate that the combination of ICB targeting the PD-1/PD-L1 signaling axis and ICD-inducing chemotherapy synergistically enhances the antitumor effects for TNBC [15–19]. The underlying mechanism may involve chemo-immunotherapy leading to the transformation of immunologically 'cold' tumors into 'hot' lesions, which are characterized by the infiltration of mature DCs and the presence of cytotoxic T lymphocytes (CTLs).

In recent years, PD-1/PD-L1 peptide-based inhibitors are gaining attention in cancer immunotherapy and tumor-targeted delivery [20–26]. Compared to monoclonal antibodies, which are most used in cancer immunotherapy, peptides offer several advantages in ligand targeting. For instance, peptides can penetrate tissues more effectively, have a lower likelihood of inducing immunogenicity, are more cost-effective to manufacture, and are easier to quality control during synthesis [9, 20, 23]. Nonetheless, peptides exhibit limitations, including low target affinity, rapid renal clearance, and susceptibility to degradation [27–29]. Thus, it is imperative to enhance the efficacy of PD-L1 antagonist peptides in blocking PD-1/PD-L1 interactions.

Azide/cyclooctyne-based bio-orthogonal chemistry occurs in vivo, while maintaining the structural integrity and biological activity [30–33]. Azides ($-N_3$), a bio-orthogonal functional group, can be metabolically incorporated into cell-surface glycoproteins [33, 34]. In contrast to the transient binding typically observed in physical interactions between ligands and endogenous receptors, azides, acting as 'chemical receptors,' demonstrate high specificity and effectiveness in binding with cyclooctyne-labeled biomolecules with long-term retention [33, 35]. Herein, making use of the recognition by anti-PD-L1 peptides and cyclooctyne/azide-based bio-orthogonal click chemistry, we propose anti-PD-L1 peptide-based biomolecules to achieve efficient and sustained PD-L1 targeting to enhance the efficacy and sustainability of ICB therapy.

In this study, we present PD-L1-targeted theranostic systems modified with PD-L1 antagonist peptide (CVRARTR; *Cys-Val-Arg-Ala-Arg-Thr-Arg*), DOTA, and dibenzocyclooctyne (DBCO). We first designed a gadolinium (Gd)-based probe APP^{Gd}-Cy7, which is decorated with fluorescent sulfo-Cyanine7 (Cy7), aiming for achieving targeted PD-L1 magnetic resonance/near-infrared fluorescence (MR/NIRF) imaging in vivo for TNBC. Then, we replaced the fluorescence imaging module of Cy7 with the drug-loading module of DOX to generate prodrug APP^{Gd}-DOX, with the goal of synergistic chemo-immunotherapy for TNBC. As illustrated in Scheme 1, TNBC cells (4T1) overexpressing PD-L1 as natural receptors were pretreated with tetraacetyl-*N*-azidoacetylmannosamine (Ac_4ManNAz) to produce azides as 'chemical receptors' on cell surfaces. APP^{Gd}-Cy7 can recognize PD-L1 expressed on 4T1 cells, followed by conjugating with azide-labeled glycoproteins on 4T1 cells via bio-orthogonal click chemistry, remarkably improving and extending MR/NIRF imaging. Following this, the prodrug APP^{Gd}-DOX accumulates in the tumor via PD-L1 targeting and covalently bind to the azide-rich tumor cell surfaces, significantly facilitating uptake and internalization of this prodrug in TNBC cells. The utilization of PD-L1 antagonist peptide conjugated prodrug facilitates the inhibition of PD-L1, thereby impeding tumor immune evasion and augmenting antitumor immunity. Additionally, the APP^{Gd}-DOX prodrug enhances drug delivery efficiency by acidic pH-responsive DOX release, evoking the ICD effect and DAMPs release, further promoting DC maturation and activation of CTLs. Consequently, the enhanced targeted delivery of APP^{Gd}-DOX prodrug demonstrated significant efficacy in inhibiting tumor growth by inducing a potent immune response against the tumor, ultimately resulting in the restoration of immune tolerance in TNBC.

Materials and methods

Agents

Lyso-Tracker, Mito-Tracker, and DiO green, DAPI solution, Hoechst 33,342 working solution (1×), and CCK-8 assay kit were sourced from Beyotime Ltd. The Millipore filtration system was utilized to purify water. Flow cytometry antibodies, including anti-CD3-APC, anti-CD4-FITC, anti-CD8-PercpCy5.5, anti-IFN-γ-PE/Cy7, anti-CD25-PE/Cy7, anti-Foxp3-V450, anti-MHC II-V450, anti-CCR7-PE, anti-CD80-FITC, and anti-CD40-APC antibodies were provided by BioLegend, Inc. Anti-PD-L1-antibody was sourced from Proteintech (Chicago, USA, 66248-1-Ig). Anti-Calreticulin, anti-HMGB1, anti-Cleaved-Caspase-3, anti-Cleaved-GSDME, and anti-GSDME antibodies were obtained from Abcam (Cambridge, MA, ab92516, ab79823, ab52101, ab222470, and ab215191). Doxorubicin hydrochloride (DOX) was obtained from Bide Pharmatech Ltd. (Shanghai, China), while Ac_4ManNAz was procured from Sigma-Aldrich (Saint Louis, USA, 900917).

Cell culture

The murine 4T1 and HC11 (mouse mammary epithelial cells) cell lines were procured from the Cell Bank of the Chinese Academy of Sciences in Shanghai, China. These cell lines were cultured in RPMI-1640 medium

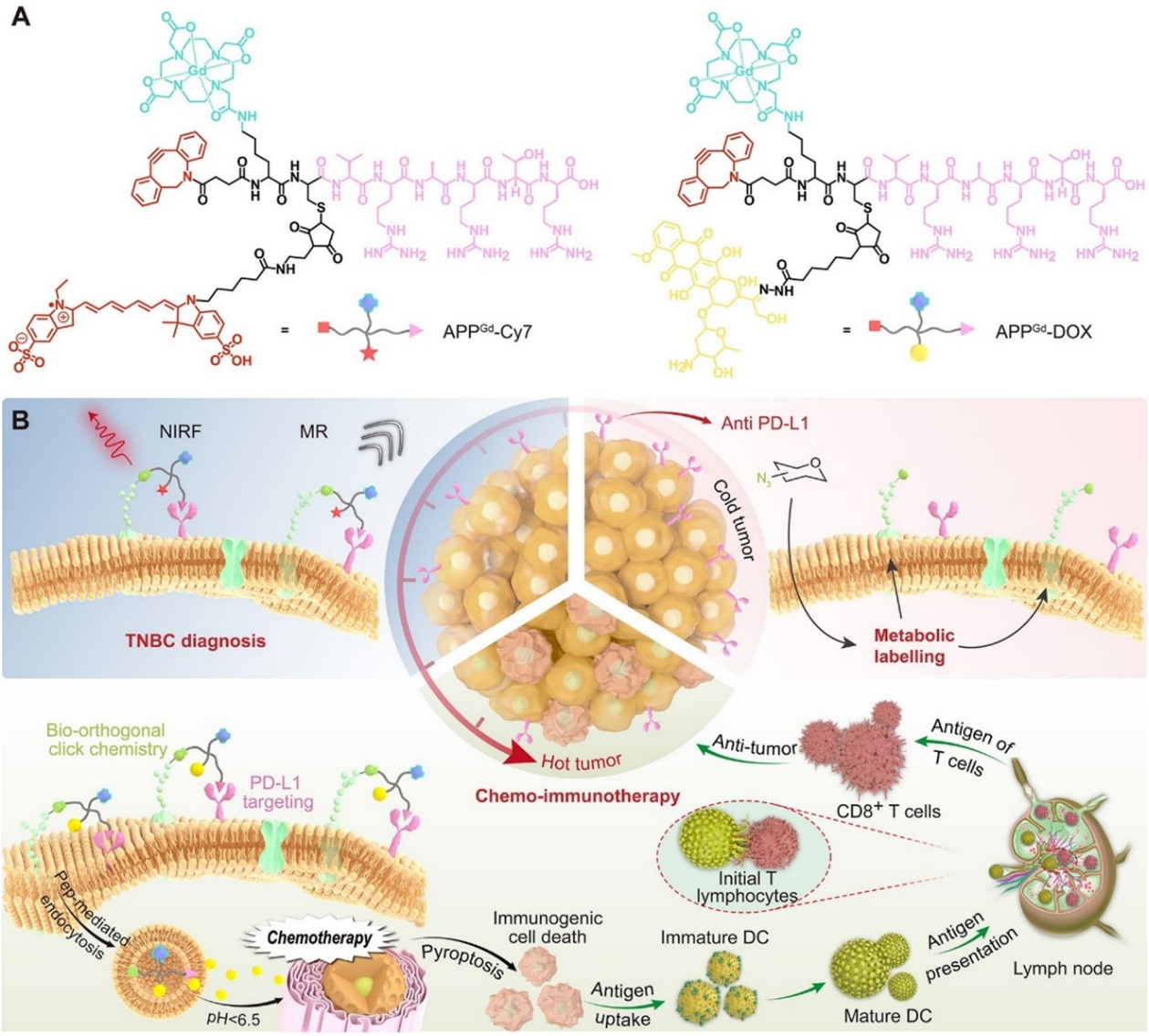

Scheme 1 Illustration of the bio-orthogonal click chemistry strategy for PD-L1-targeted imaging and pyroptosis-mediated chemo-immunotherapy of TNBC. **A** Chemical structure of PD-L1-targeted probe APP^{Gd}-Cy7 and prodrug APP^{Gd}-DOX. **B** In vivo MR/NIRF imaging process involves metabolism glycoengineering, and the PD-L1 targeting accumulation of APP^{Gd}-Cy7 in tumor tissue; In vivo synergistic chemo-immunotherapy strategy includes metabolism glycoengineering, PD-L1 targeting, and pH-responsive drug release and pyroptosis-mediated regulation of antitumor immunity

supplemented with 10% fetal bovine serum and 1% penicillin–streptomycin solution at 37 °C in a 5% CO_2 humidified environment.

Synthesis of APP^{Gd}-Cy7, APP^{Gd}-Cy5, and APP^{Gd}-DOX

The peptide was produced on a rink amide resin (loading: 0.81 mmol/g) with the assistance of a CEM Liberty one microwave-assisted peptide synthesizer. Following the attachment of all amino acids and DOTA, the resultant products were transferred to a glass peptide synthesis vessel. Following deprotection of the Fmoc group, the compounds were conjugated with *N*-succinimidyl 4-[(5-aza-3,4:7,8-dibenzocyclooct-1-yne)-5-yl]-4-oxobutyrate (DBCO-NHS). After conjugation of DBCO, the resultant product was dissociated from its solid support through treatment using a cleavage cocktail composed of trifluoroacetic acid-triisopropylsilane-H_2O (95:2.5:2.5). Subsequently, the solution was eliminated, and the resulting white solids were precipitated by adding dry diethyl ether, followed by centrifugation at a speed of ~ 6500 rpm for ~ 15 min. The peptide was subsequently purified and isolated using preparative high-performance

liquid chromatography (HPLC) with a C-18 column. The compounds APP^{Gd}-Cy7 and APP^{Gd}-Cy5 were synthesized by coordinating gadolinium (Gd) ions with the DOTA chelator on APP and then conjugating them with fluorescent Cy7 or sulfo-cyanine 5 (Cy5) through a thiol-maleimide reaction. Similarly, the prodrug APP^{Gd}-DOX was prepared by labeling with Gd^{3+} ions and conjugating with the 6-maleimidocaproylhydrazone derivative of doxorubicin (Mal-DOX) using a thiol-maleimide reaction.

Physical characterization and drug release profile

The ^{1}H nuclear magnetic resonance (^{1}H-NMR) and attenuated total reflectance Fourier transform infrared (ATR FT-IR) spectrum of APP, APP^{Gd}-Cy5, APP^{Gd}-Cy7 and APP^{Gd}-DOX were obtained at room temperature with a Bruker ADVANCE NEO 600 MHz NMR spectrometer and a Nicolet 6700 FTIR spectrometer, respectively. The absorption and fluorescence spectra of APP^{Gd}-Cy7, APP^{Gd}-Cy5 and APP^{Gd}-DOX were assessed at varying concentrations (2.5–10 μM). The cumulative release of DOX was evaluated through dialysis of the APP^{Gd}-DOX prodrug in phosphate-buffered saline (PBS) at varying pH levels (7.4, 6.5, 6.0, and 5.0). Dialysis was conducted using a dialysis tube with a molecular weight cutoff (MWCO) of 1000 for a duration of 10 h. The release of DOX was monitored by measuring absorbance values at 490 nm using a UV–visible spectrometer (Varian Cary 100 Conc).

Cellular uptake and colocalization analysis

4T1 cells were treated with APP^{Gd}-Cy5 (10 μM) following a 3-day incubation with 50 μM Ac_4ManNAz, and subsequently stained with DAPI to visualize the cell nucleus. To examine intracellular distribution, 4T1 cells were exposed to APP^{Gd}-Cy5 (10 μM) for 4 h, followed by staining with 5 μM DiO green, 50 nM Lyso-Tracker green or 100 nM Mito-Tracker green for 30 min, and Hoechst33342 working solution (1×) for an additional 15 min as per standard protocol. Following washes with PBS twice, fluorescence imaging was conducted utilizing a confocal laser scanning microscope (CLSM, Leica TCS SP5, Germany). The cellular uptake of DOX was assessed in 4T1 cells following treatment with DOX, APP^{Gd}-DOX, and Click-APP^{Gd}-DOX at a concentration of 2 μM.

In vitro cytotoxicity assay

To assess the cytotoxicity of Ac_4ManNAz, 4T1 and HC11 cells were cultured in 96-well plates and incubated with varying concentrations of Ac_4ManNAz (0–50 μM) for a duration of three days. Subsequently, cell viability was subsequently assessed using a CCK-8 assay. Following this, the same cells were cultured with either 0 or 50 μM Ac_4ManNAz for three days in 96-well plates, and then treated with DOX and APP^{Gd}-DOX at different concentrations (0–10 μM) for a period of 24 h. Cell viability was evaluated again using the CCK-8 assay.

Western blot analysis of cells

4T1 cells were exposed to either 0 or 50 μM Ac_4ManNAz for a duration of 3 days, subsequently treated with different agents (DOX, APP, and APP^{Gd}-DOX) at a uniform concentration of 2 μM for a period of 24 h. A protease inhibitor-supplemented RIPA buffer was used to lyse the cells following treatments. The expression levels of PD-L1, CRT, HMGB1, GSDME-FL, GSDME-N, and Cleaved Caspase-3 were then evaluated through western blot analysis.

RNA sequencing

4T1 cells were collected following treatment with or without APP^{Gd}-DOX, and total RNA was extracted for RNA sequencing. The resulting transcriptomic sequencing data was analyzed and visualized utilizing an online platform available at https://www.bioinformatics.com.cn. All genes with an adjusted p-value < 0.05 and fold change > 1.5 were considered significant.

Animal experiment

Female BALB/c mice, 5–6 weeks old, were sourced from the Shanghai Experimental Animal Center and kept in a pathogen-free facility. All animal experiments followed approved guidelines from the Ethics Committee of Xinhua Hospital, affiliated with Shanghai Jiao Tong University School of Medicine (XHEC-F-2023-014). Subcutaneous injections of 1.0×10^{6} 4T1 cells suspended in 100 μL PBS were administered to each mouse on the flanks.

In vivo and ex vivo fluorescence (FL) imaging

Mice were divided into three groups (n = 3 per group): PEG-Cy7, APP^{Gd}-Cy7, and Click-APP^{Gd}-Cy7. Prior to this, mice with 4T1 tumors received intraperitoneal injections of either 40 mg/kg Ac_4ManNAz once daily for 3 days or were injected with PBS. Subsequently, the cohorts were intravenously injected with 1 mg/kg PEG-Cy7 or 1 mg/kg APP^{Gd}-Cy7. Under isoflurane anesthesia, in vivo fluorescence imaging of the 4T1 tumor-bearing mice was carried out using the IVIS spectrum system (PerkinElmer), with excitation at 710 nm and emission collected at 760 ± 20 nm. Imaging and analysis of the mice were conducted at specific time points.

In vivo MR imaging

Following the formation of the subcutaneous tumor, Ac_4ManNAz (40 mg/kg) was administered intraperitoneally once daily for three days to the Click-APP^{Gd}-Cy7

group (n = 3). The Gd-DOTA and APP^{Gd}-Cy7 groups (n = 3 per group) received PBS injections as the control. Subsequently, mice with 4T1 tumors were intravenously injected with Gd-DOTA (150 μL, 1 mg/kg) or APP^{Gd}-Cy7 (150 μL, 1 mg/kg). Magnetic resonance images were obtained prior to the injection of Gd-DOTA or APP^{Gd}-Cy7, as well as at 1-, 2-, 3-, and 4-h(s) post-injection.

Antitumor activity

After reaching a subcutaneous tumor volume of approximately 150 mm^3, 4T1 tumor-bearing mice were randomly assigned to five groups (n = 5 per group): (1) PBS, (2) DOX, (3) APP^{Gd}-DOX, (4) Click-APP, and (5) Click-APP^{Gd}-DOX. In the click groups, $Ac_4ManNAz$ (40 mg/kg) was administered intraperitoneally once daily for 3 days, while other groups received PBS injections. Subsequently, all groups were treated every seven days with PBS, DOX, APP, or APP^{Gd}-DOX (5 mg/kg). Body weights and tumor volumes were measured every two days for 14 days. Tumor volume (V) was calculated according to the formula: $V\ (mm^3) = 0.5 \times L\ (mm) \times W^2\ (mm^2)$.

Histological examination

Fresh tumors and organs were fixed in 4% paraformaldehyde, embedded in paraffin, and sectioned for various analyses, including H&E staining, immunohistochemical staining, and immunofluorescence staining. For immunofluorescence staining, primary antibodies against PD-L1, CRT, HMGB1, Caspase-3, CD4, and CD8 were utilized. The process involved deparaffinization, heat-induced antigen retrieval using a citrate solution, and blocking with 5% BSA. The samples were subjected to overnight incubation with primary antibodies at 4 ℃, followed by a 1-h incubation with secondary antibodies at room temperature. DAPI was utilized as a nuclear counterstain for immunofluorescence staining.

Flow cytometry analysis, HMGB1 release, and cytokine assay

Following various treatments, spleens, tumors, and tumor-draining lymph nodes (TDLNs) from all experimental groups (n = 5 per group) were excised and subsequently subjected to enzymatic digestion using collagenase IV at 37 °C for a duration of 1 h. The digested tissues were subsequently filtered through a 70 μm cell strainer to obtain single-cell suspensions. These isolated single cells were then suspended in a staining buffer and labeled with fluorescent-conjugated antibodies to identify specific cell populations, including CTLs ($CD3^+CD4^-CD8^+$), $CD4^+$T cells ($CD3^+CD4^+CD8^-$), mature DCs ($CD40^+CD80^+$MHC $II^+CCR\ 7^+$), and Tregs ($CD4^+CD25^+Foxp3^+$). Enzyme-linked immunosorbent assay (ELISA) kits were employed to quantify the levels of HMGB1, IFN-γ, TNF-α, and IL-12 in serum specimens obtained from mice following different treatments.

Statistics

Quantitative values were presented as mean ± standard deviation (SD), and statistical analyses were conducted using a two-tailed Student's t-test and one-way ANOVA. A significance level of $P < 0.05$ was employed to determine statistical significance, denoting a distinction between the groups under comparison.

Results and discussion

Preparation and characterization of APP^{Gd}-Cy5, APP^{Gd}-Cy7 and APP^{Gd}-DOX

The APP modified with 1,4,7,10-tetraazacyclododecane-1,4,7,10-tetraacetic acid (DOTA) was synthesized via conventional Fmoc-based solid-phase peptide (SPPS) methodology, as illustrated in Fig. 1A. Characterization of the isolated APP was conducted utilizing high-performance liquid chromatography (HPLC) and mass spectrometry (Figures S1 and S2). For MR/fluorescence imaging purposes, the compounds APP^{Gd}-Cy5 and APP^{Gd}-Cy7 were prepared by labeling the peptide with gadolinium (Gd) ions through coordination with the DOTA chelator, followed by conjugation with fluorescent sulfo-cyanine 5 (Cy5) or sulfo-cyanine7 (Cy7) using a thiol-maleimide reaction (Scheme 1A and Fig. 1B). Similarly, the compound APP^{Gd}-DOX prodrug was labeled with Gd^{3+} ions and the acid-labile hydrazone bond-linked Mal-DOX using a thiol-maleimide reaction (Scheme 1A). The chemical structures of APP, APP^{Gd}-Cy5, APP^{Gd}-Cy7 and APP^{Gd}-DOX were further characterized by ^{1}H-NMR and ATR FT-IR spectrum (Figures S3–S10). Absorbance and fluorescence spectra of the labeled compounds, including APP^{Gd}-Cy5, APP^{Gd}-Cy7, and APP^{Gd}-DOX, were analyzed in PBS (pH 7.4). The absorption and fluorescence peaks of APP^{Gd}-Cy5 were observed at ~ 650 nm and 670 nm, respectively (Fig. 1C, D). APP^{Gd}-Cy7 exhibited absorbance at 750 nm and strong fluorescence intensity at 780 nm, facilitating enhanced photon penetration through tissues while minimizing the impact of tissue autofluorescence (Fig. 1E, F). Moreover, the absorbance of APP^{Gd}-DOX was noted at 480 nm, with a low fluorescence intensity detected at 610 nm (Fig. 1G, H).

Given that DOX was linked to APP^{Gd}-DOX through an acid-labile hydrazone bond, it is expected to exhibit pH-sensitive release within endo/lysosomal environments (pH ~ 5.0). To assess this, the pH-responsive degradation kinetics of APP^{Gd}-DOX were quantitatively analyzed using dialysis tubes with a molecular weight cutoff of 1000 Da in PBS at varying pH levels (7.4, 6.5, 6.0, and 5.0). Analysis depicted in Fig. 1I revealed minimal DOX

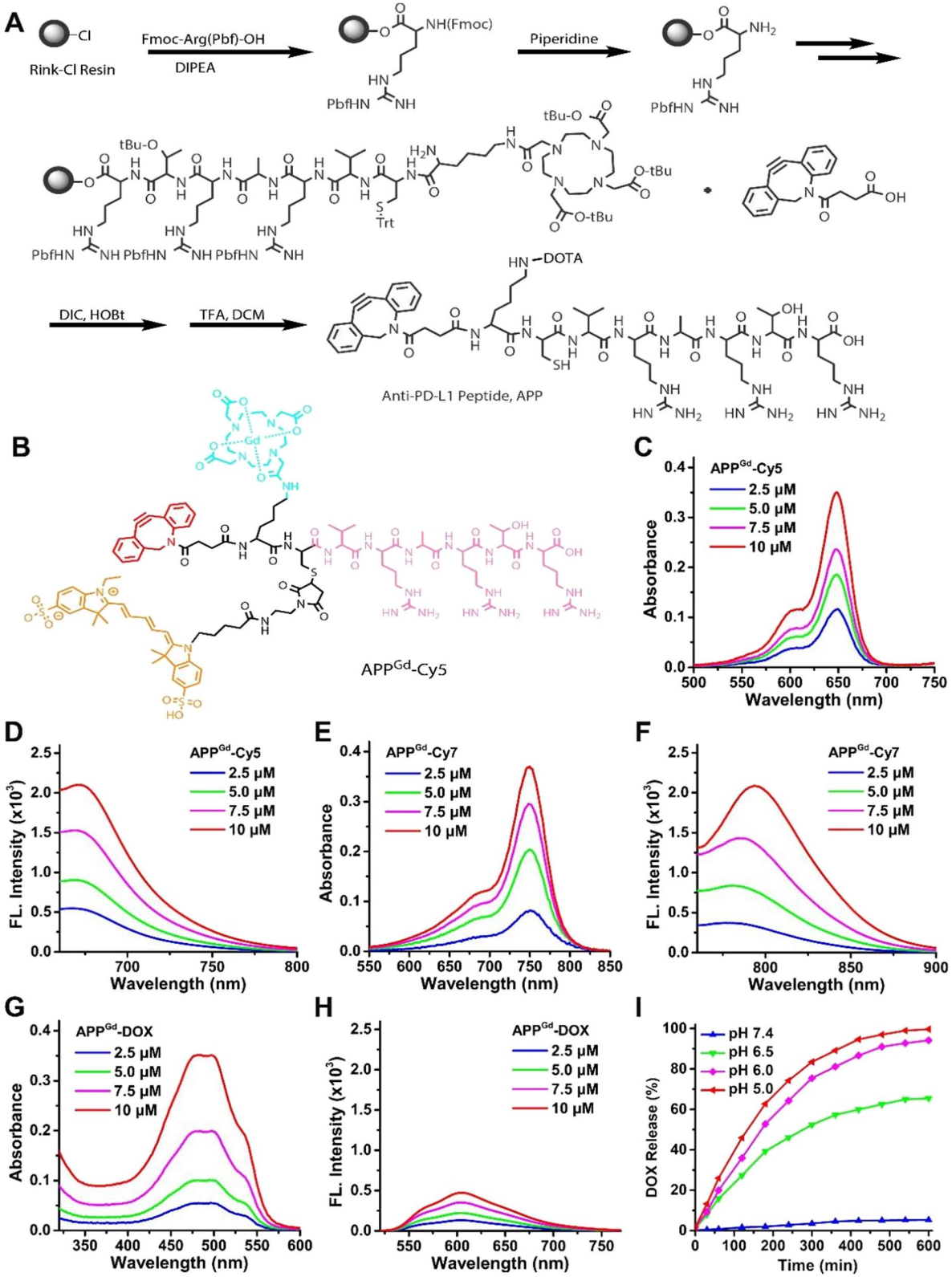

Fig. 1 Preparation and characterization of APP^{Gd}-Cy5, APP^{Gd}-Cy7, and APP^{Gd}-DOX prodrug. **A** Schematic synthesis route of APP. **B** Chemical structure of APP^{Gd}-Cy5. **C–H** The absorption and fluorescence spectra of APP^{Gd}-Cy5, APP^{Gd}-Cy7, and APP^{Gd}-DOX prodrug at various concentrations (2.5–10 μM). **I** The cumulative release of DOX from the APP^{Gd}-DOX prodrug was observed following incubation at pH levels of 7.4, 6.5, 6.0, and 5.0, respectively

release (~ 5%) from APP^{Gd}-DOX over 600 min in PBS at pH 7.4, suggesting the robust stability of the prodrug in physiological condition. In contrast, the activation of APP^{Gd}-DOX demonstrated rapid kinetics, leading to the release of over 60% and 90% of DOX after 10 h of incubation in PBS at pH levels of 6.5 and 6.0, respectively. Conversely, near 100% of DOX was released from APP^{Gd}-DOX at pH 5.0 within the same time, highlighting the sensitivity of APP^{Gd}-DOX to endo-/lysosomal pH. This characteristic suggests that APP^{Gd}-DOX has the potential to minimize premature drug release and reduce adverse effects in healthy tissues, while facilitating targeted intracellular drug delivery, thereby offering significant advantages in cancer treatment.

In vitro cellular uptake and cytotoxicity evaluation

We first labeled 4T1 cells with azide groups by treating them with 50 μM Ac_4ManNAz. Subsequently, Ac_4ManNAz-pretreated 4T1 cells were incubated with 10 μM APP^{Gd}-Cy5. The uptake efficiency of APP^{Gd}-Cy5 reflected variations in the formation of azides. After incubation with APP^{Gd}-Cy5, Ac_4ManNAz-pretreated 4T1 cells exhibited a 2.52 ± 0.16-fold higher fluorescence intensity compared to non-pretreated 4T1 cells (Fig. 2A, B). We also conducted azide group labeling on HC11 cells using Ac_4ManNAz pretreatment. Following incubation with APP^{Gd}-Cy5, Ac_4ManNAz-pretreated HC11 cells exhibited a weaker fluorescence intensity compared to non-pretreated 4T1 cells (Fig. 2A, B), indicating PD-L1 targeting for 4T1 cells. Overall, in Ac_4ManNAz-pretreated 4T1 cells, the click efficiency of APP^{Gd}-Cy5 with azide groups significantly increased. This enhanced click efficiency suggests promising potential for tumor-targeted drug delivery. We further investigated the subcellular organelle localization behavior of APP^{Gd}-Cy5 in Ac_4ManNAz-pretreated 4T1 cells, and the results were quantified utilizing ImageJ. As illustrated in Fig. 2E, F a substantial amount of APP^{Gd}-Cy5 was internalized into lysosomes. A notable degree of co-localization between APP^{Gd}-Cy5 (red) and lysosomes (green) was observed in Ac_4ManNAz-pretreated 4T1 cells following a 4-h incubation period. Additionally, the fluorescence intensity of DOX showed a 3.42 ± 0.28-fold increase in Click-APP^{Gd}-DOX, and a 1.85 ± 0.13-fold increase in APP^{Gd}-DOX than in DOX (Fig. 2C, D). Substantial anti-PD-L1 peptide was internalized into lysosomes. Recent studies have highlighted that the controlled targeting of PD-L1 for lysosomal degradation is pivotal in preventing the undesirable recycling of PD-L1 [36, 37]. Consequently, the intracellular disposition of APP^{Gd}-DOX has been shown to enhance the lysosomal degradation of PD-L1, thereby potentially increasing its therapeutic efficacy. Furthermore, APP^{Gd}-DOX specifically releases DOX and accumulated in 4T1 cells, amplifying the enhanced cytotoxicity of DOX.

We further examined the cytotoxicity of Ac_4ManNAz and observed no significant harm to normal HC11 cells and 4T1 cells at concentrations up to 50 μM (Fig. 2G). Subsequently, we evaluated the cytotoxic effects of DOX, APP^{Gd}-DOX, and Click-APP^{Gd}-DOX in HC11 and 4T1 cells. As shown in Fig. 2H, DOX displayed non-selective cytotoxicity, with comparable levels of toxicity observed in both cell types. As illustrated in Fig. 2I, APP^{Gd}-DOX demonstrated an enhanced cytotoxic response against 4T1 cells at a concentration of 2 μM, compared to DOX alone. This enhanced response is attributed to the PD-L1 targeting effect of APP^{Gd}-DOX, which allows for killing 4T1 cells at relatively low drug doses, thereby minimizing non-specific cytotoxicity. Furthermore, Click-APP^{Gd}-DOX exhibited more potent tumor cell-specific cytotoxicity than APP^{Gd}-DOX at the same concentration of 2 μM, suggesting that the bio-orthogonal click chemistry strategy enhances PD-L1-targeted delivery efficacy.

In vitro PD-L1 binding

Western blotting was used to assess the expression level of PD-L1 in vitro. 4T1 cells exhibited a higher PD-L1 level compared to murine mammary epithelial HC11 cells (Figure S3). Several pre-clinical and clinical studies demonstrated PD-L1 as a potently promising target for TNBC [8, 16, 38–40]. DOX treatment also induced an elevation in PD-L1 expression of 4T1 cells [41, 42], resulting in exhaustion of T cells and immune tolerance, key components of tumor immune escape [43–47]. In addition, several studies have revealed a significant upregulation of PD-L1 protein levels in tumor specimens derived from TNBC patients following DOX chemotherapy, which is beneficial for enhancing the efficacy of PD-1/PD-L1 blockade immunotherapy [38, 48]. The mechanism of PD-L1 upregulation after DOX chemotherapy may include inflammatory signaling [49], the DNA damage response pathway [50], activation of NF-κB pathway [51], and oxidative stress [52]. Nevertheless, the administration of APP^{Gd}-DOX in Ac_4ManNAz-pretreated 4T1 cells showed reduced PD-L1 expression levels compared to the control group (Fig. 3E). CVRARTR, a peptide antagonist of PD-L1, serves as a promising alternative to monoclonal antibodies for ICB, which has been widely studied in recent years [20, 37, 53, 54]. The internalization-induced downregulation of PD-L1 by binding peptides not only directly impedes the binding of PD-L1 but also indirectly augments their efficacy in inhibiting the PD-1/PD-L1 interaction by reducing the cell surface availability of PD-L1 [20, 37]. Therefore, we speculate that the binding of anti-PD-L1-Peptide (CVRARTR) to PD-L1-overexpressing cells is specifically mediated

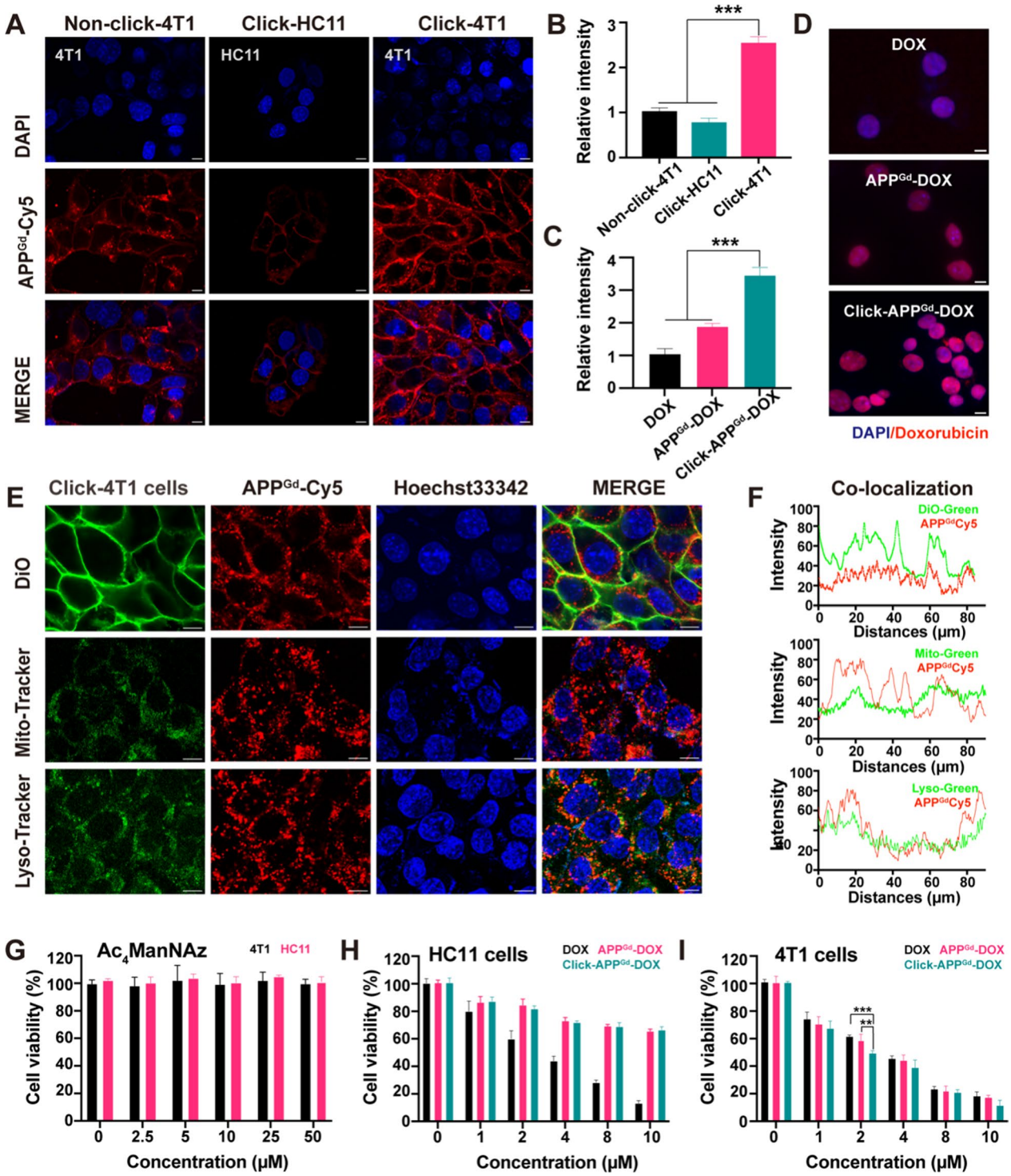

Fig. 2 **A** CLSM images of APP^{Gd}-Cy5 (10 μM) in 4T1 cells treated with either 0 or 50 μM Ac_4ManNAz (Non-click-4T1 or Click-4T1), and HC11 cells treated with 50 μM Ac_4ManNAz (Click-HC11). **B** Relative FL intensities of APP^{Gd}-Cy5 (10 μM) in 4T1 cells treated with either 0 or 50 μM Ac_4ManNAz, and HC11 cells treated with 50 μM Ac_4ManNAz. (**C**) Relative FL intensities and (**D**) fluorescence images of DOX in 4T1 cells incubated with DOX, APP^{Gd}-DOX, and Click-APP^{Gd}-DOX (2 μM). DOX. **E** CLSM images of 4T1 cells treated with 10 μM APP^{Gd}-Cy5, co-stained with 5 μM DiO, or 100 nM Mito-Tracker or 50 nM Lyso-Tracker green. **F** Co-localization curves. Scale bars: 10 μm. Cell viabilities of (**G**) HC11 and 4T1 cells treated with Ac_4ManNAz, (**H**) HC11 cells or (**I**) 4T1 cells treated with DOX, APP^{Gd}-DOX, and Click-APP^{Gd}-DOX

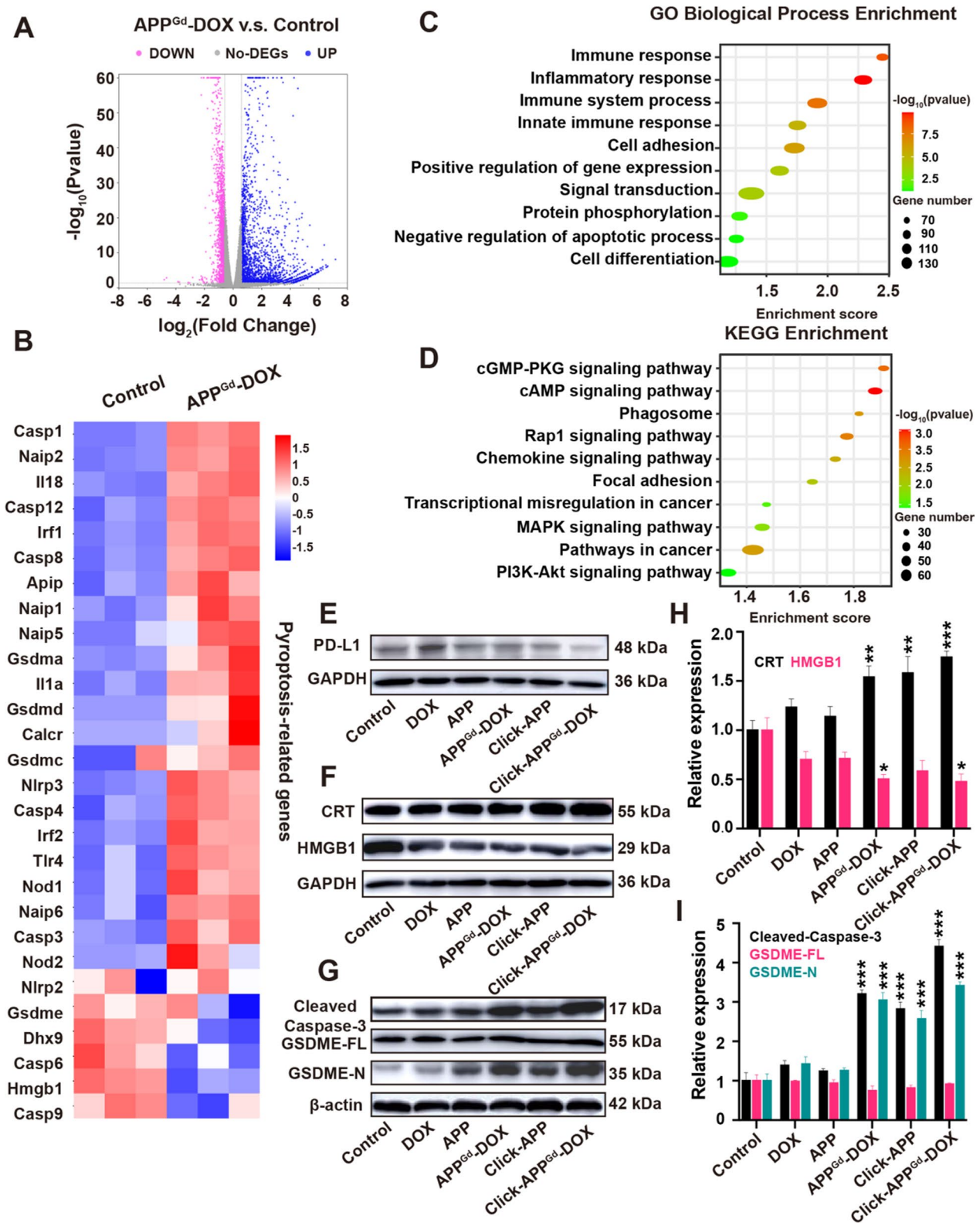

Fig. 3 **A** Volcano plot of DEGs, (**B**) heatmap to visualize the expression of pyroptosis-related genes, (**C**) GO biological process analyses of DEGs, and (**D**) KEGG analyses of DEGs in the control *vs* APP^{Gd}-DOX. **E–I** Western blot analysis of PD-L1, CRT, HMGB1, Cleaved-caspase-3, GSDME-FL, and GSDME-N in 4T1 cells after treatments with Control, DOX, APP, APP^{Gd}-DOX, Click-APP, and Click-APP^{Gd}-DOX, respectively. *$P < 0.05$, **$P < 0.01$, and ***$P < 0.001$ *vs* Control group

through PD-L1, and the downregulation of PD-L1 to the inhibition of PD-L1 by PD-L1-binding peptides.

Evaluation of ICD and pyroptosis in vitro

RNA sequencing of 4T1 cells was conducted following APP^{Gd}-DOX treatment. Comparative analysis with the control group revealed 3781 differentially expressed transcripts in the APP^{Gd}-DOX group, with 1439 downregulated and 2342 upregulated. These differentially expressed genes (DEGs) are displayed on a standard volcano plot (Fig. 3A). The Gene Ontology (GO) function analysis histogram, presented in Figure S13, delineates biological process, cellular ingredients, and molecular functions. GO analysis within the biological processes category (Fig. 3C) revealed enrichment in genes related to immune response, immune system processes, and innate immune responses. KEGG pathway analysis (Fig. 3D) indicated enrichment in proteins associated with pathways in cancer, cAMP signaling, MAPK signaling, and PI3K-Akt signaling. The enrichment of genes in these pathways indicates that pyroptosis plays a complex role across a range of biological processes. Pyroptosis aids in the removal of harmful pathogens and cells that have been compromised, and it also has the capacity to modulate inflammatory pathways, which could have implications for the behavior of tumors.

The immunogenicity of ICD is predominantly facilitated by DAMPs, including exposed CRT on cell surfaces, secreted ATP, and released HMGB1 [55]. These DAMPs, generated during ICD, can interact with pattern recognition receptors on the surface of DCs, initiating a cascade of cellular responses. These responses ultimately lead to the activation of immune responses, thereby augmenting the effectiveness of immunotherapy. Several studies have provided evidence that immune response against tumors can be augmented by ICD in conjunction with ICB therapy [14, 56, 57]. Moreover, the presence of CRT on cell surfaces and the release of HMGB1 from the nucleus are considered hallmarks signifying the induction of ICD. To substantiate our hypothesis and probe the mechanisms involved, we conducted western blot analysis in vitro to assess the expression of CRT and HMGB1, as indicators of ICD. Figure 3F, H suggests that upon treatment with Click-APP^{Gd}-DOX, there is a marked increase in CRT exposure in 4T1 cells, along with a noticeable decrease in intracellular HMGB1 secretion, potentially indicating substantial release from the nucleus. This implies that the combination of chemo-immunotherapy and biorthogonal click chemistry strategies could achieve a potent synergistic therapeutic effect, resulting in significant induction of ICD and enhancing TNBC's immunogenicity.

Furthermore, Pyroptosis, a newly identified form of programmed cell death with unique morphological traits distinct from those of apoptosis and necrosis, is capable of inducing the release of antigens and subsequently triggering potent antigen-specific immune responses [58]. A heatmap displaying DEGs related to pyroptosis in vitro after APP^{Gd}-DOX was generated by transcriptomic analysis (Fig. 3B). Western blot analysis was further conducted to validate the occurrence of pyroptosis in vitro. Given that Caspase-3 precisely cleaves the middle linker of gasdermin E (GSDME) to generate the GSDME-N domain, subsequently triggering pyroptosis through the formation of membrane pores, Cleaved-Caspase-3 level and GSDME expression levels were assessed in response to various in vitro treatments [59]. As displayed in Fig. 3G, I, the Cleaved Caspase-3 showed a notable elevation in the Click-APP^{Gd}-DOX group. Similarly, GSDME-N was observed in Click-APP^{Gd}-DOX treated cells and exhibited the highest expression level. These findings affirm the ability of Click-APP^{Gd}-DOX to trigger Caspase-3-mediated GSDME-dependent pyroptosis in tumor cells.

In vivo and ex vivo for FL imaging

To assess enhanced tumor retention and biodistribution, in vivo FL imaging of mice with 4T1 tumors was conducted in three groups (n = 3): (1) PEG-Cy7, (2) APP^{Gd}-Cy7, and (3) Click-APP^{Gd}-Cy7. Upon reaching a tumor volume approximately 150 mm^3, the group receiving click-containing treatment were intraperitoneally injected with Ac_4ManNAz (40 mg/kg) daily for 3 days. Subsequently, mice were intravenously administered 150 μL (1 mg/kg) of PEG-Cy7 and APP^{Gd}-Cy7 via the tail vein. Using the IVIS spectrum, we recorded selected time points from 1 h to 14 days post-injection, as depicted in Fig. 4A. Compared to PEG-Cy7, mice injected with APP^{Gd}-Cy7 and Click-APP^{Gd}-Cy7 displayed significantly higher fluorescence signals during the imaging period, demonstrating prolonged tumor retention and efficient accumulation of PD-L1 targeting. Additionally, the fluorescence signals in Click-APP^{Gd}-Cy7 were the highest among the three groups, showing 4.00–15.81 times and 1.21–2.48 times higher signals compared to PEG-Cy7 and APP^{Gd}-Cy7 after injection, respectively (Fig. 4D). These results confirm the effective bio-orthogonal click reaction and PD-L1 targeting function to gain favorable retention of the APP^{Gd}-Cy7 in the tumor.

To compare organ distribution in 4T1 tumor-bearing mice, tumors and major organs were excised on day 14, and the fluorescence intensity from excised organs and tumor tissues were measured using the IVIS spectrum. As illustrated in Fig. 4B, E, tumor retention of Click-APP^{Gd}-Cy7 group was the highest than the other two groups. Furthermore, the fluorescence intensities of tumors in Click-APP^{Gd}-Cy7 group were greatly higher

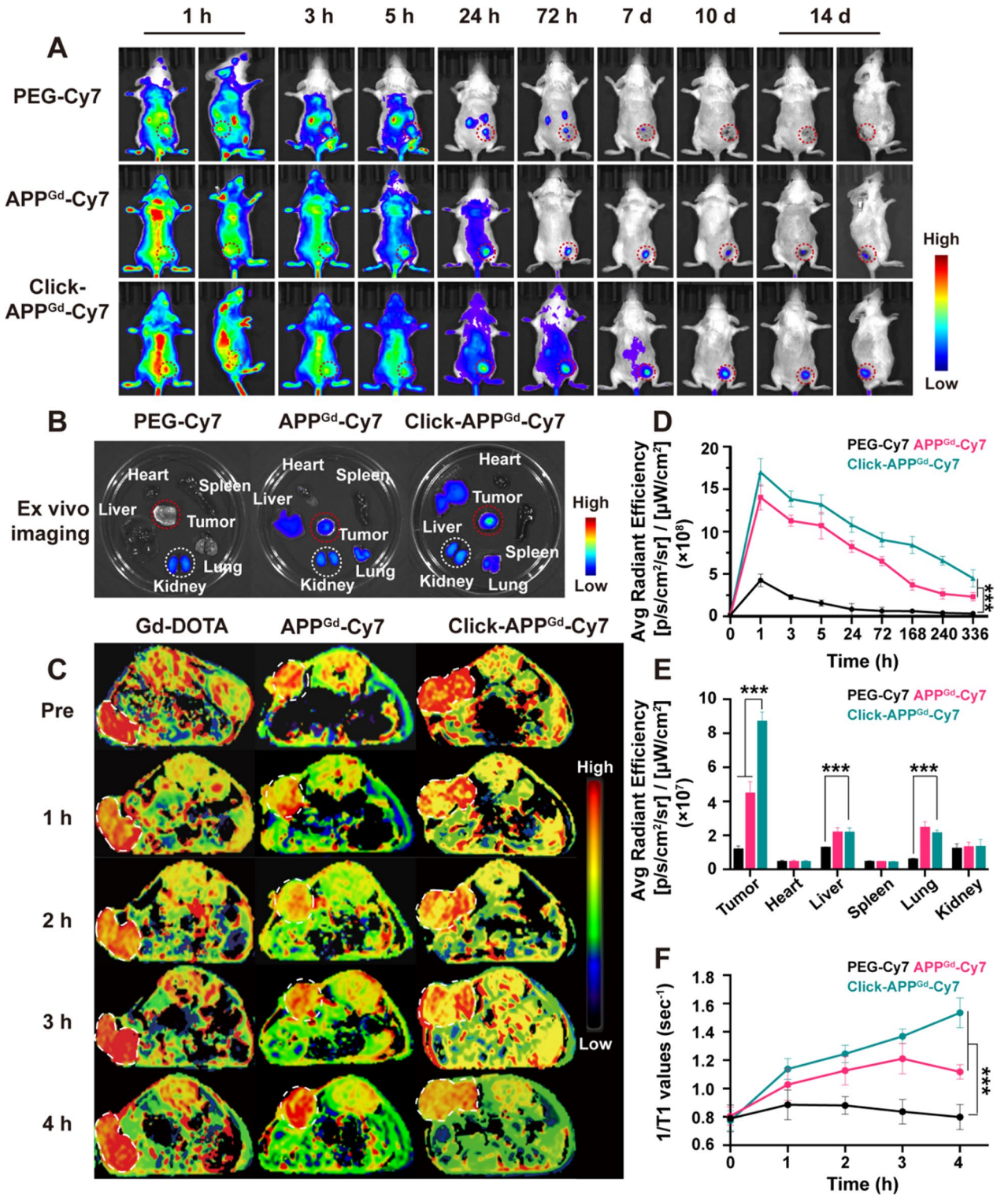

Fig. 4 **A** In vivo FL imaging after injection of PEG-Cy7, APP^{Gd}-Cy7, or Click-APP^{Gd}–Cy7. **B** Ex vivo FL imaging. **C** In vivo MR-T1 mapping images of mice after injection of Gd-DOTA, APP^{Gd}-Cy7, or Click-APP^{Gd}–Cy7. **D** FL intensities in tumor regions and (**E**) ex vivo FL intensities of organs and tumors. **F** Time-dependent 1/T1 changes in MR-T1 mapping images after injection of Gd-DOTA, APP^{Gd}-Cy7, and Click-APP^{Gd}–Cy7. ***$P < 0.001$

compared to those in other tissues, such as the liver and kidneys, suggesting excellent retention and distribution efficiency within the tumor. Besides, the fluorescence signals of Click-APP^{Gd}-Cy7 and APP^{Gd}-Cy7 in liver and lungs were only surpassed by those in the tumor. We hypothesize that PD-L1 is highly expressed on cancer cells and macrophages, while macrophages are predominantly found in organs such as the liver and lungs [46].

In vivo MR-T1 mapping imaging

Subsequently, in vivo MR-T1 mapping imaging was performed on 4T1-tumor-bearing mice, randomly divided into 3 groups (n = 3 per group): (1) Gd-DOTA, (2) APP^{Gd}-Cy7, (3) Click-APP^{Gd}-Cy7, as depicted in Fig. 4C. At 1- and 2-h post-injection, all three groups exhibited enhanced tumor signals. By 3 h post-injection, signals in the Gd-DOTA group had returned to baseline levels, while signal enhancement continued in the Click-APP^{Gd}-Cy7 and APP^{Gd}-Cy7 groups. Furthermore, the signal enhancement in the APP^{Gd}-Cy7 reduced at 4-h post-injection, whereas Click-APP^{Gd}-Cy7 continued to exhibit sustained enhancement. To quantitatively evaluate the signal intensities of tumor retention, 1/T1 values were measured and illustrated in Fig. 4F. The 1/T1 values in both the Click- and non-click-APP^{Gd}-Cy7 groups consistently exceeded those in the Gd-DOTA group post-injection, indicating the enhanced active PD-L1 targeting. Furthermore, the highest 1/T1 values in Click-APP^{Gd}-Cy7 at 4-h post-injection were 1.98-times higher compared to the baseline scale, while the highest 1/T1 values in APP^{Gd}-Cy7 at 3 h post-injection were 1.39-times higher compared to the baseline scale. These results from in vivo MR-T1 mapping imaging and the change in 1/T1 values demonstrate the reliable and prolonged tumor retention in the Click-APP^{Gd}-Cy7 group, highlighting efficient click reactions and enhanced PD-L1 targeting.

Antitumor efficacy in vivo

Encouraged by the favorable in vitro antitumor activity and improved in vivo tumor retention, we subsequently evaluated the therapeutic efficacy of different treatments in vivo. As illustrated in Fig. 5A, 4T1 tumor-bearing mice were randomly assigned into five groups (n = 5 per group): (1) i.v. PBS, (2) i.v. DOX, (3) i.v. APP^{Gd}-DOX, (4) i.p. Ac_4ManNAz-treated (40 mg/kg) + i.v. APP, and (5) Ac_4ManNAz-treated (40 mg/kg) + i.v. APP^{Gd}-DOX, at a dose of 5 mg/kg. Initially, all groups exhibited gradual increases in body weights, except for the DOX group, which experienced severe weight loss due to in vivo systemic toxicity (Fig. 5D). Compared to the PBS group, DOX exhibited a modest 50.00% decrease in tumor growth, suggesting restricted therapeutic effectiveness with a single administration of chemotherapy (Fig. 5B). In contrast, both APP^{Gd}-DOX and Click-APP exhibited significant delays in tumor growth, achieving reductions of 67.49% and 71.79%, respectively, after treatment. Notably, Click-APP^{Gd}-DOX demonstrated the most profound antitumor effect, achieving an approximately 86.12% inhibition of tumor growth. This enhanced antitumor efficacy of Click-APP^{Gd}-DOX can be attributed to improved tumor accumulation facilitated by efficient bio-orthogonal click chemistry and enhanced PD-L1 targeting, as well as synergistic chemo-immunotherapy.

Tumor weights and photos at the end of treatments are displayed in Fig. 5C. The Click-APP^{Gd}-DOX group decreased to 23.58% compared to the PBS control group and 29.83% compared to the DOX-treated group, indicating a substantial tumor inhibition rate of 76.42%. H&E analysis revealed significant therapeutic effects, including extensive cellular atrophy and nuclear condensation after Click-APP^{Gd}-DOX therapy (Fig. 5E). The TUNEL assay and Caspase-3 immunofluorescence staining confirmed effective tumor eradication within the Click-APP^{Gd}-DOX group (Fig. 5F, G, Figure S14A, B). Additionally, the Click-APP^{Gd}-DOX markedly downregulated the PD-L1 expression in tumor cells (Fig. 5H and Figure S14C), indicating effective PD-L1 blockade. Moreover, evaluation of treatment-related toxicity through H&E analyses on major organs showed substantial damage in the DOX group compared to PBS-treated mice, while only negligible structural abnormalities were observed in APP^{Gd}-DOX, Click-APP^{Gd}, and Click-APP^{Gd}-DOX groups (Figure S15). In summary, the enhanced tumor-targeted delivery of APP^{Gd}-DOX using bio-orthogonal click chemistry and PD-L1 targeting demonstrated synergistic chemo-immunotherapy, resulting in the inhibition of tumor progression. Moreover, Click-APP^{Gd}-DOX mitigated off-target toxicity associated with chemotherapeutic drugs.

In vivo ICD and immune response induced by Click-APP^{Gd}−DOX

The in vivo ICD effect induced by Click-APP^{Gd}-DOX was assessed through immunofluorescence staining and the ELISA kit, as shown in Fig. 6A, Figure S14D, E and Figure S16. Consistent with the observed antitumor effect, the Click-APP^{Gd}-DOX group exhibited the highest levels of CRT expression and the most substantial release of HMGB1 among all the treated groups. This result could be explained by the heightened accumulation of DOX at the tumor site, leading to enhanced DAMPs release and presentation for DC recruitment, which is crucial for initiating immune responses [60, 61].

Mature DCs, functioning as a major subset of antigen-presenting cells (APCs), aid in presenting tumor associated antigens to T cells, thereby initiating T cell

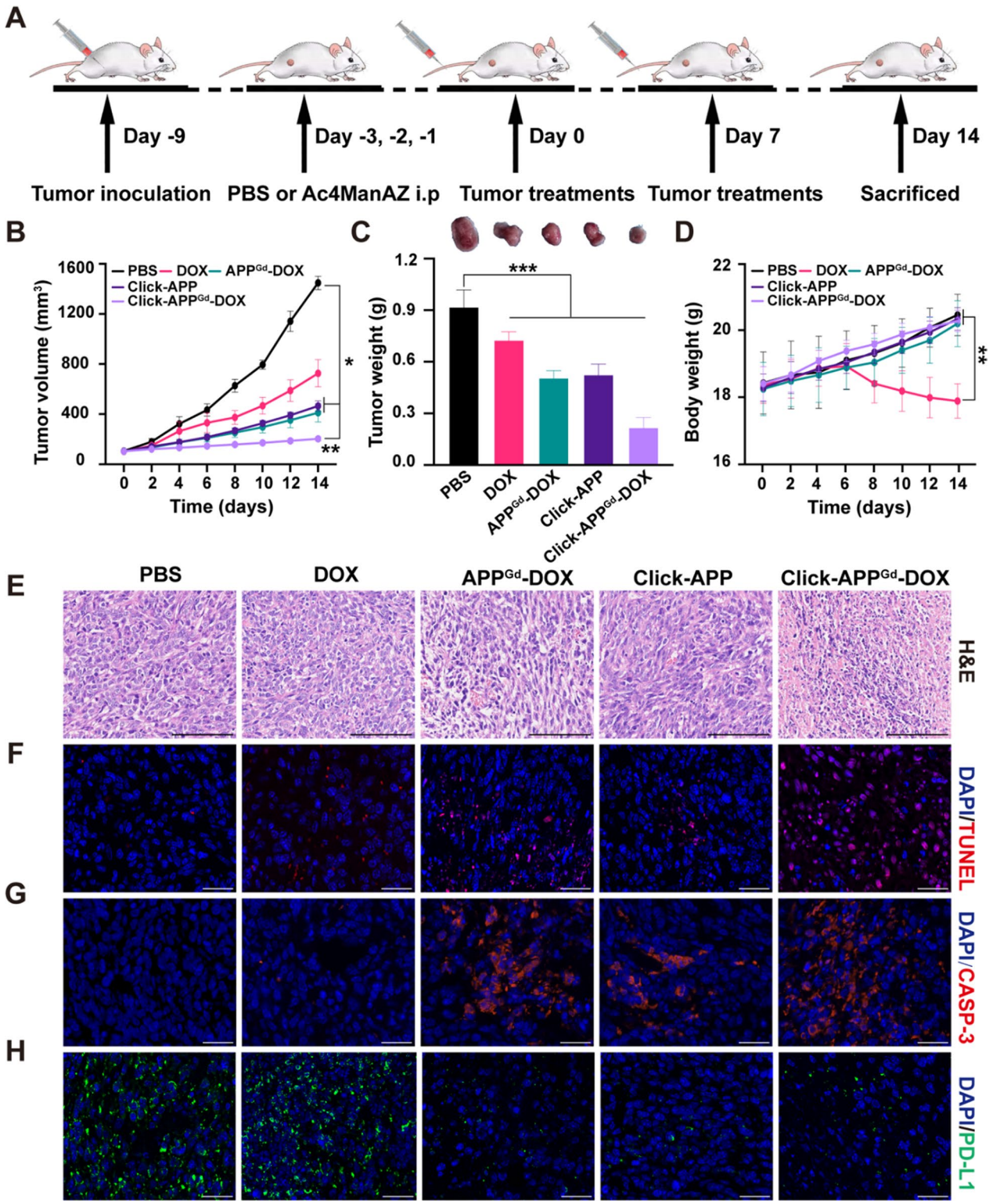

Fig. 5 **A** Illustration of 4T1 tumor inoculation and therapeutic interventions in BALB/c mice. **B** Body weights, (**C**) tumor volume, (**D**) tumor weights and tumor photos after various treatments, including (1) PBS, (2) DOX, (3) APP^{Gd}-DOX, (4) Click-APP, and (5) Click-APP^{Gd}-DOX. $^{**}P < 0.01$ and $^{***}P < 0.001$. **E–H** Representative H&E staining, TUNEL, Caspase-3, and PD-L1 immunofluorescence staining of tumor slides. Scale bar: 100 μm

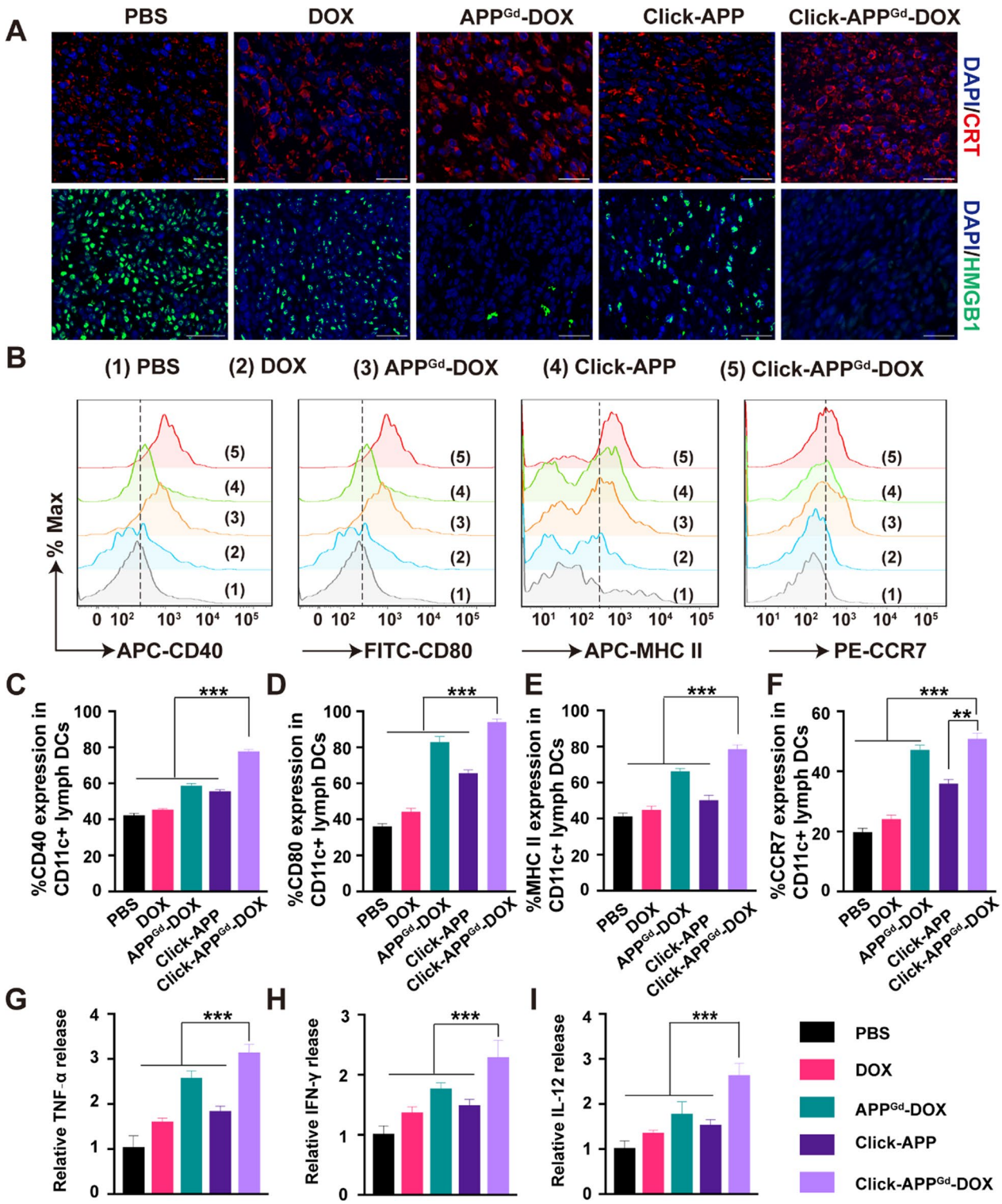

Fig. 6 Click-APP^{Gd}-DOX induced ICD, DC maturation, and proinflammatory cytokine secretion in vivo. **A** Representative tumor sections of CRT, and HMGB1 immunofluorescence staining. Scale bar is 100 μm. **B** Markers including CD40, CD80, MHC II, and CCR7 on the DC membrane from TDLNs in groups treated with (1) PBS, (2) DOX, (3) APP^{Gd}-DOX, (4) Click-APP, and (5) Click-APP^{Gd}-DOX groups were evaluated by flow cytometry. **C–F** Quantification of CD40, CD80, MHC II and CCR7. Relative concentration of the (**G**) TNF-α, (**H**) IFN-γ, and (**I**) IL-12. $^{**}P < 0.01$ and $^{***}P < 0.001$

activation [62–65]. To evaluate the maturation of DCs in vivo, cells obtained TDLNs were stained with fluorescently labeled antibodies targeting CD80, CD40, MHC II, and CCR7, followed by analyses using flow cytometry. In comparison to the PBS group, the levels of costimulatory molecules CD40 and CD80 were obviously elevated in the APP^{Gd}-DOX and Click-APP^{Gd}-DOX groups (Fig. 6B). CD40 and CD80 expression levels in the Click-APP^{Gd}-DOX groups were 1.85 and 2.59 times higher, respectively, than in the PBS group (Fig. 6C, D). Major histocompatibility complex class II (MHC II) molecules are essential for capturing peptides in the endocytic pathway to produce T cell receptor ligands, facilitating the maturation of DCs [66, 67]. Click-APP^{Gd}-DOX groups induced 78.70 ± 2.25% of MHC-II expression in TDLNs, significantly higher than that of APP^{Gd}-DOX (66.38 ± 1.41%), Click-APP (50.34 ± 2.63%), or DOX (45.04 ± 1.85%) (Fig. 6E). C–C chemokine receptor 7 (CCR7) guides mature DCs from the peripheral tissues to lymph nodes, regulating T cell activation and adaptative immunity [68, 69]. As shown in Fig. 6F, Click-APP^{Gd}-DOX facilitated the highest level of CCR7 expression, demonstrating a 1.08-fold increase compared to APP^{Gd}-DOX, a 1.41-fold increase compared to Click-APP, and a 2.10-fold increase compared to DOX. These findings underscore the potent capability of matured DC migration. In summary, the above results collectively demonstrate that the combination of the bio-orthogonal click chemistry strategy and synergistic chemo-immunotherapy promotes the maturation and migration of DCs.

The levels of circulating cytokines TNF-α, IFN-γ, and IL-12 were quantified using ELISA, as shown in Fig. 6I. Both the APP^{Gd}-DOX and Click-APP^{Gd}-DOX formulations demonstrated significant elevations in TNF-α, IFN-γ, and IL-12 concentrations within TME, indicative of heightened activity of TILs producing these cytokines. Specifically, the relative levels of TNF-α, IFN-γ, and IL-12 in the Click-APP^{Gd}-DOX group were approximately 1.22-fold, 1.30-fold, and 1.49-fold higher than those in the APP^{Gd}-DOX group, respectively, suggesting a robust antitumor immune response.

Subsequently, infiltration of T cells is investigated by immunofluorescence staining, as depicted in Figure S17. Fluorescence signals detected in the Click-APP^{Gd}-DOX group highlight a substantial infiltration of $CD8^+$ T cells and a comparatively lower presence of regulatory T cells (Tregs) in the tumor, underscoring the potential for activating antitumor immunity. To further explore the in vivo immunoregulatory effects, we conducted flow cytometry analyses CTLs, $CD4^+$ T cells, Tregs, and tumor-infiltrating T cells (TILs) (Figure S18). Mature DCs, assisting in antigen presentation to naïve T lymphocytes, effectively initiate the activation of CTLs, ultimately leading to tumor rejection [70]. Figure 7A, E demonstrate a statistically notable increase in the proportion of CTLs in the Click-APP^{Gd}-DOX-treated group (28.08 ± 0.81%) compared to the PBS control group (22.76 ± 0.71%), in accordance with the results obtained through immunofluorescence staining. Moreover, the $CD8^+/CD4^+$ T cell ratio within the $CD3^+$ lymphocyte subset serves as a crucial indicator of adaptive T cell immunity, with a decrease in this ratio frequently associated with unfavorable outcomes in immunotherapy. Compared to the PBS group (0.32 ± 0.02%), the Click-APP^{Gd}-DOX-treated group (0.43 ± 0.02%) exhibited a noteworthy increase in the $CD8^+/CD4^+$ T cell ratio (Fig. 7F), indicating a significant improvement. This enhancement is primarily attributed to the infiltration of CTLs into TME. The percentage of intratumoral CTL infiltration notably increased from 0.819 ± 0.02% in the PBS group to 3.274 ± 0.05% in the Click-APP^{Gd}-DOX group, indicating a substantial improvement facilitated by Click-APP^{Gd}-DOX in intratumoral CTL infiltration (Figure S19 and Fig. 7G). Consequently, the combination of bio-orthogonal click chemistry and chemo-immunotherapy effectively increases CTL infiltration and demonstrates robust systemic immune activation.

Tregs constitute a critical component of the TME, exerting immunosuppressive effects on antitumor immunity [71, 72]. As displayed in Fig. 7B, H, the proportion of splenic Tregs in the group treated with APP^{Gd}-DOX (11.00 ± 0.94%) was markedly reduced compared to both the PBS group (21.28 ± 0.88%) and the DOX group (14.98 ± 1.14%). Moreover, the Tregs percentage in the group treated with Click-APP^{Gd}-DOX (7.47 ± 0.66%) was significantly lower compared to both the groups treated with APP^{Gd}-DOX (11.00 ± 0.94%) and Click-APP (11.78 ± 0.93%). Furthermore, the presence of $CD3^+CD8^+CD25^+Foxp^{3+}$ Treg (T8regs) cells was also examined. As depicted in Figure S20, Click-APP^{Gd}-DOX demonstrated a 3.41% reduction in $CD8^+$ Tregs in comparison to the control group treated with PBS. This observation suggest that Click-APP^{Gd}-DOX depletes $CD8^+$ Treg cells effectively. In addition to enhancing the proliferation of CTLs, the treatment with Click-APP^{Gd}-DOX exhibited the potential to suppress immunosuppressive Tregs.

CD28, a crucial costimulatory molecule expressed on $CD8^+$ T cells, exerts a significant influence on the activity of effector T cells [73]. As depicted in Figure S21 and Fig. 7I, the Click-APP^{Gd}-DOX group (7.78 ± 0.09%) exhibited a notable increase in the proportion of $CD28^+$ cells among the $CD3^+CD8^+$ T cell subset compared to the PBS group (4.31 ± 0.16%). This enhancement contributes to the improved function of effector T cells and bolster immune responses. IFN-γ^+ CTLs facilitate

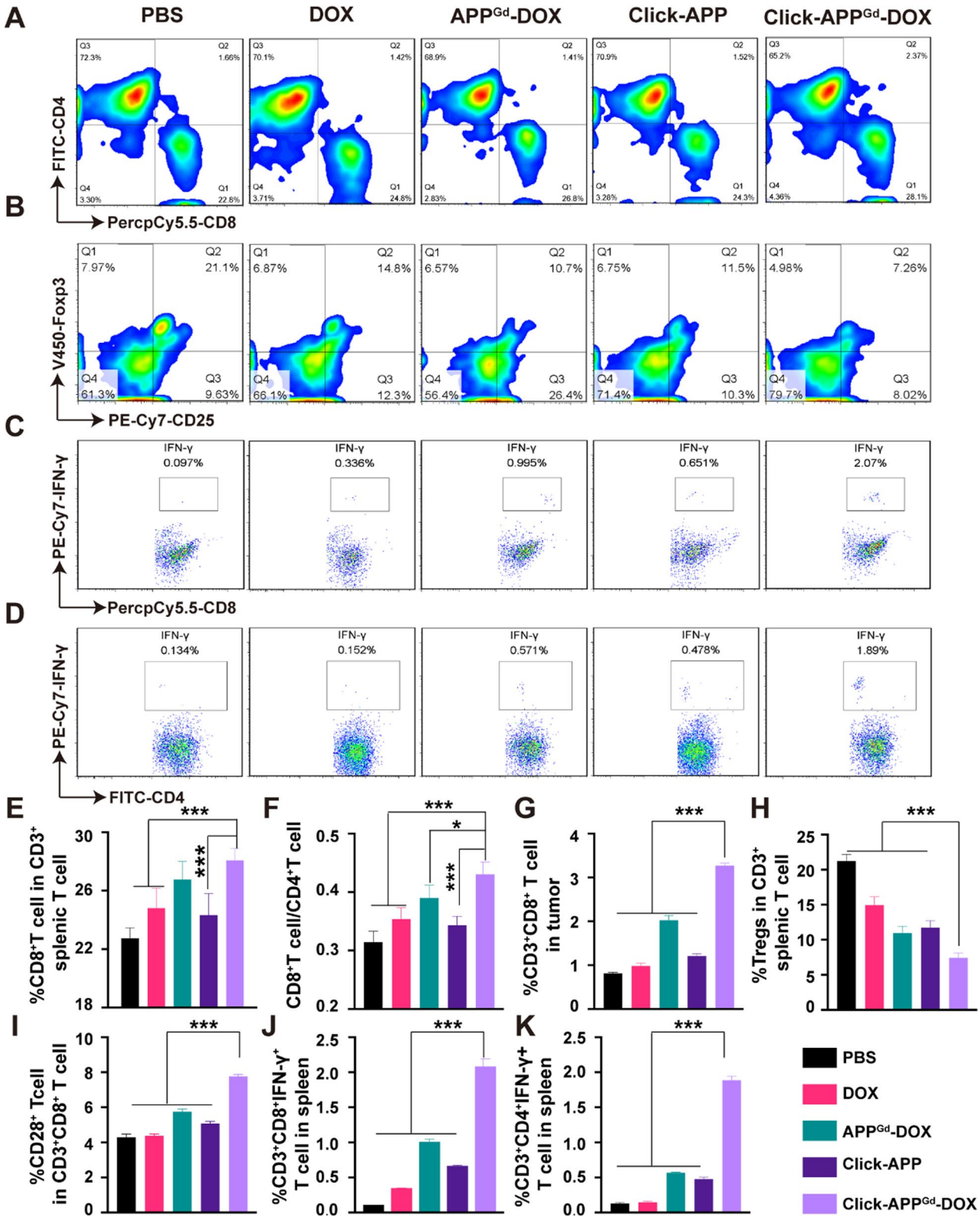

Fig. 7 T cell immune responses were assessed in vivo following treatment with (1) PBS, (2) DOX, (3) APP^{Gd}-DOX, (4) Click-APP, and (5) Click-APP^{Gd}-DOX. Representative flow cytometry analyses of (**A**) CD4$^+$ and CD8$^+$ splenic T cells, **B** splenic Tregs, (**C**) splenic IFN-γ$^+$CD8$^+$ T cells, and (**D**) splenic IFN-γ$^+$ CD4$^+$ T cells. **E** Percentage of CTLs in splenic CD3$^+$ T cells. **F** The ratio of CD8$^+$/CD4$^+$ T cells. **G** Percentages of intratumoral CD3$^+$CD8$^+$ T cells, **H** Tregs in splenic CD3$^+$ T cells, (**I**) CD28$^+$ T cells in CD3$^+$CD8$^+$ splenic T cells, **J** splenic IFN-γ$^+$ CD8$^+$ T cells, and (**K**) splenic CD4$^+$IFN-γ$^+$ T cells. *$P < 0.05$, **$P < 0.01$, and ***$P < 0.001$

the differentiation of $CD8^+$ T cells into antigen-specific CTLs, while IFN-γ^+ CD4 + T cells support the differentiation of $CD4^+$ T cells into Th1 cells [74]. Flow cytometry analyses were conducted to assess these phenomena, as shown in Fig. 7C, D. In comparison to the PBS group (0.10 ± 0.01%), the percentage of IFN-$\gamma^+CD3^+CD8^+$ T cells in the Click-APP^{Gd}-DOX (2.07 ± 0.12%) demonstrated a statistically significant increase (Fig. 7J). Furthermore, Click-APP^{Gd}-DOX displayed the highest proportion of IFN-$\gamma^+CD3^+CD4^+$ T cells, exhibiting a 3.95-, 3.31-, and 12.45-fold increase when compared to APP^{Gd}-DOX, Click-APP, or DOX, respectively (Fig. 7K).

Conclusion

In summary, we have developed the bio-orthogonal muti-functional theranostic system using bio-orthogonal click chemistry and PD-L1 targeting strategy. Following the administration of Ac_4ManNAz, tumor cells efficiently introduced azide groups on their cell surfaces, subsequently engaging bio-orthogonal click reactions with DBCO-modified theranostic system. APP^{Gd}-Cy7 achieve enhanced and prolonged MR/NIRF imaging in vivo for PD-L1 targeting of TNBC. Furthermore, the APP^{Gd}-DOX prodrug with PD-L1 targeting performs pH-responsive DOX release, inducing ICD and DAMPs release in tumor cells, thereby initiating robust antitumor immune responses, and attracting various immune cells to the TME. The combination of ICB with the ICD-inducing chemotherapy could mitigate the suppressive influence of tumor cells on the antitumor immune response, leading to a significant reduction in tumor growth. Overall, our study presents a promising approach utilizing bio-orthogonal click chemistry, PD-L1 targeting, and pH-responsive drug release for combined MR/NIRF imaging and synergistic chemo-immunotherapy in TNBC.

Supplementary Information

The online version contains supplementary material available at https://doi.org/10.1186/s12951-024-02727-7.

Supplementary Material 1.

Acknowledgements
This work was supported by the National Natural Science Foundation of China (82071870, 92159203, 81901870), the Sponsored Program of Shanghai Science and Technology Committee (No. 21S31905000), the Shanghai Rising-Star Program (22QA1406000) and Natural Science Foundation of Shanghai (21ZR1441600).

Author contributions
Author contributions Yan Wang: Validation, Investigation, Visualization, Writing-original draft. Yanhong Chen, Yuelin Huang, Weixi Huang, and Xue Dong: Validation, Visualization. Ding-Kun Ji: Methodology, Investigation. Defan Yao: Conceptualization, Methodology, Investigation, Formal analysis, Writing—review and editing, Funding acquisition. Dengbin Wang: Supervision, Writing—review and editing, Project administration, Funding acquisition. All authors read and approved the final manuscript.

Data availability
No datasets were generated or analysed during the current study.

Declarations

Ethics approval and consent to participate
Laboratory animal ethical and welfare committee of XinHua Hospital Affiliated to Shanghai JiaoTong University School of Medicine, approved the animal experiment protocol (XHEC-F-2024-014).

Competing interests
The authors declare no competing interests.

Author details
[1]Department of Radiology, Xinhua Hospital, Shanghai Jiao Tong University School of Medicine, Shanghai 200092, China. [2]College of Health Science and Technology, Shanghai Jiao Tong University School of Medicine, Shanghai 200025, China. [3]Institute of Molecular Medicine (IMM), Renji Hospital, Shanghai Jiao Tong University School of Medicine, Shanghai 200240, China.

Received: 4 May 2024 Accepted: 17 July 2024
Published online: 01 August 2024

References

1. Keenan TE, Tolaney SM. Role of immunotherapy in triple-negative breast cancer. J Natl Compr Canc Netw. 2020;18(4):479–89.
2. Pardoll DM. The blockade of immune checkpoints in cancer immunotherapy. Nat Rev Cancer. 2012;12(4):252–64.
3. Bagchi S, Yuan R, Engleman EG. Immune checkpoint inhibitors for the treatment of cancer: clinical impact and mechanisms of response and resistance. Annu Rev Pathol. 2021;16:223–49.
4. Sun C, Mezzadra R, Schumacher TN. Regulation and Function of the PD-L1 Checkpoint. Immunity. 2018;48(3):434–52.
5. Marin-Acevedo JA, Kimbrough EO, Lou Y. Next generation of immune checkpoint inhibitors and beyond. J Hematol Oncol. 2021;14(1):45.
6. Waldman AD, Fritz JM, Lenardo MJ. A guide to cancer immunotherapy: from T cell basic science to clinical practice. Nat Rev Immunol. 2020;20(11):651–68.
7. Beckers RK, Selinger CI, Vilain R, Madore J, Wilmott JS, Harvey K, Holliday A, Cooper CL, Robbins E, Gillett D, et al. Programmed death ligand 1 expression in triple-negative breast cancer is associated with tumour-infiltrating lymphocytes and improved outcome. Histopathology. 2016;69(1):25–34.
8. Mittendorf EA, Philips AV, Meric-Bernstam F, Qiao N, Wu Y, Harrington S, Su X, Wang Y, Gonzalez-Angulo AM, Akcakanat A, et al. PD-L1 expression in triple-negative breast cancer. Cancer Immunol Res. 2014;2(4):361–70.
9. Maute RL, Gordon SR, Mayer AT, McCracken MN, Natarajan A, Ring NG, Kimura R, Tsai JM, Manglik A, Kruse AC, et al. Engineering high-affinity PD-1 variants for optimized immunotherapy and immuno-PET imaging. Proc Natl Acad Sci USA. 2015;112(47):E6506–14.
10. Casares N, Pequignot MO, Tesniere A, Ghiringhelli F, Roux S, Chaput N, Schmitt E, Hamai A, Hervas-Stubbs S, Obeid M, et al. Caspase-dependent immunogenicity of doxorubicin-induced tumor cell death. J Exp Med. 2005;202(12):1691–701.
11. Lau TS, Chan LKY, Man GCW, Wong CH, Lee JHS, Yim SF, Cheung TH, McNeish IA, Kwong J. Paclitaxel induces immunogenic cell death in ovarian cancer via TLR4/IKK2/SNARE-dependent exocytosis. Cancer Immunol Res. 2020;8(8):1099–111.
12. Tesniere A, Schlemmer F, Boige V, Kepp O, Martins I, Ghiringhelli F, Aymeric L, Michaud M, Apetoh L, Barault L, et al. Immunogenic death of colon cancer cells treated with oxaliplatin. Oncogene. 2010;29(4):482–91.
13. Galluzzi L, Humeau J, Buque A, Zitvogel L, Kroemer G. Immunostimulation with chemotherapy in the era of immune checkpoint inhibitors. Nat Rev Clin Oncol. 2020;17(12):725–41.

14. Duan X, Chan C, Lin W. Nanoparticle-mediated immunogenic cell death enables and potentiates cancer immunotherapy. Angew Chem Int Ed Engl. 2019;58(3):670–80.
15. Cortes J, Rugo HS, Cescon DW, Im SA, Yusof MM, Gallardo C, Lipatov O, Barrios CH, Perez-Garcia J, Iwata H, et al. Pembrolizumab plus chemotherapy in advanced triple-negative breast cancer. N Engl J Med. 2022;387(3):217–26.
16. Schmid P, Adams S, Rugo HS, Schneeweiss A, Barrios CH, Iwata H, Diéras V, Hegg R, Im SA, Shaw Wright G, et al. Atezolizumab and nab-paclitaxel in advanced triple-negative breast cancer. N Engl J Med. 2018;379(22):2108–21.
17. Schmid P, Cortes J, Pusztai L, McArthur H, Kummel S, Bergh J, Denkert C, Park YH, Hui R, Harbeck N, et al. Pembrolizumab for early triple-negative breast cancer. N Engl J Med. 2020;382(9):810–21.
18. Mittendorf EA, Zhang H, Barrios CH, Saji S, Jung KH, Hegg R, Koehler A, Sohn J, Iwata H, Telli ML, et al. Neoadjuvant atezolizumab in combination with sequential nab-paclitaxel and anthracycline-based chemotherapy versus placebo and chemotherapy in patients with early-stage triple-negative breast cancer (IMpassion031): a randomised, double-blind, phase 3 trial. Lancet. 2020;396(10257):1090–100.
19. Loibl S, Untch M, Burchardi N, Huober J, Sinn BV, Blohmer JU, Grischke EM, Furlanetto J, Tesch H, Hanusch C, et al. A randomised phase II study investigating durvalumab in addition to an anthracycline taxane-based neoadjuvant therapy in early triple-negative breast cancer: clinical results and biomarker analysis of GeparNuevo study. Ann Oncol. 2019;30(8):1279–88.
20. Gurung S, Khan F, Gunassekaran GR, Yoo JD, Poongkavithai Vadevoo SM, Permpoon U, Kim SH, Kim HJ, Kim IS, Han H, et al. Phage display-identified PD-L1-binding peptides reinvigorate T-cell activity and inhibit tumor progression. Biomaterials. 2020;247: 119984.
21. Chang HN, Liu BY, Qi YK, Zhou Y, Chen YP, Pan KM, Li WW, Zhou XM, Ma WW, Fu CY, et al. Blocking of the PD-1/PD-L1 interaction by a D-peptide antagonist for cancer immunotherapy. Angew Chem Int Ed Engl. 2015;54(40):11760–4.
22. Hu C, Song Y, Zhang Y, He S, Liu X, Yang X, Gong T, Huang Y, Gao H. Sequential delivery of PD-1/PD-L1 blockade peptide and IDO inhibitor for immunosuppressive microenvironment remodeling via an MMP-2 responsive dual-targeting liposome. Acta Pharm Sin B. 2023;13(5):2176–87.
23. Liu H, Zhao Z, Zhang L, Li Y, Jain A, Barve A, Jin W, Liu Y, Fetse J, Cheng K. Discovery of low-molecular weight anti-PD-L1 peptides for cancer immunotherapy. J Immunother Cancer. 2019;7(1):270.
24. Li C, Zhang N, Zhou J, Ding C, Jin Y, Cui X, Pu K, Zhu Y. Peptide blocking of PD-1/PD-L1 interaction for cancer immunotherapy. Cancer Immunol Res. 2018;6(2):178–88.
25. Magiera-Mularz K, Skalniak L, Zak KM, Musielak B, Rudzinska-Szostak E, Berlicki Ł, Kocik J, Grudnik P, Sala D, Zarganes-Tzitzikas T, et al. Bioactive macrocyclic inhibitors of the PD-1/PD-L1 immune checkpoint. Angew Chem Int Ed Engl. 2017;56(44):13732–5.
26. Song S, Shim MK, Yang S, Lee J, Yun WS, Cho H, Moon Y, Min JY, Han EH, Yoon HY, Kim K. All-in-one glycol chitosan nanoparticles for co-delivery of doxorubicin and anti-PD-L1 peptide in cancer immunotherapy. Bioact Mater. 2023;28:358–75.
27. Zaman R, Islam RA, Ibnat N, Othman I, Zaini A, Lee CY, Chowdhury EH. Current strategies in extending half-lives of therapeutic proteins. J Control Release. 2019;301:176–89.
28. Cicero AFG, Fogacci F, Colletti A. Potential role of bioactive peptides in prevention and treatment of chronic diseases: a narrative review. Br J Pharmacol. 2017;174(11):1378–94.
29. Blanco-Miguez A, Gutierrez-Jacome A, Perez-Perez M, Perez-Rodriguez G, Catalan-Garcia S, Fdez-Riverola F, Lourenco A, Sanchez B. From amino acid sequence to bioactivity: the biomedical potential of antitumor peptides. Protein Sci. 2016;25(6):1084–95.
30. Koo H, Lee S, Na JH, Kim SH, Hahn SK, Choi K, Kwon IC, Jeong SY, Kim K. Bioorthogonal copper-free click chemistry in vivo for tumor-targeted delivery of nanoparticles. Angew Chem Int Ed Engl. 2012;51(47):11836–40.
31. Moses JE, Moorhouse AD. The growing applications of click chemistry. Chem Soc Rev. 2007;36(8):1249–62.
32. Yi W, Xiao P, Liu X, Zhao Z, Sun X, Wang J, Zhou L, Wang G, Cao H, Wang D, Li Y. Recent advances in developing active targeting and multi-functional drug delivery systems via bioorthogonal chemistry. Signal Transduct Target Ther. 2022;7(1):386.
33. Yang Y, Xu J, Sun Y, Mo L, Liu B, Pan X, Liu Z, Tan W. Aptamer-based logic computing reaction on living cells to enable non-antibody immune checkpoint blockade therapy. J Am Chem Soc. 2021;143(22):8391–401.
34. Wang H, Sobral MC, Zhang DKY, Cartwright AN, Li AW, Dellacherie MO, Tringides CM, Koshy ST, Wucherpfennig KW, Mooney DJ. Metabolic labeling and targeted modulation of dendritic cells. Nat Mater. 2020;19(11):1244–52.
35. Willems LI, van der Linden WA, Li N, Li KY, Liu N, Hoogendoorn S, van der Marel GA, Florea BI, Overkleeft HS. Bioorthogonal chemistry: applications in activity-based protein profiling. Acc Chem Res. 2011;44(9):718–29.
36. Cheng K, Ding Y, Zhao Y, Ye S, Zhao X, Zhang Y, Ji T, Wu H, Wang B, Anderson GJ, et al. Sequentially responsive therapeutic peptide assembling nanoparticles for dual-targeted cancer immunotherapy. Nano Lett. 2018;18(5):3250–8.
37. Moon Y, Shim MK, Choi J, Yang S, Kim J, Yun WS, Cho H, Park JY, Kim Y, Seong JK, Kim K. Anti-PD-L1 peptide-conjugated prodrug nanoparticles for targeted cancer immunotherapy combining PD-L1 blockade with immunogenic cell death. Theranostics. 2022;12(5):1999–2014.
38. Sun M, Shi W, Wu Y, He Z, Sun J, Cai S, Luo Q. Immunogenic nanovesicle-tandem-augmented chemoimmunotherapy via efficient cancer-homing delivery and optimized ordinal-interval regime. Adv Sci (Weinh). 2022;10(1): e2205247.
39. Gilad Y, Eliaz Y, Yu Y, Han SJ, O'Malley BW, Lonard DM. Drug-induced PD-L1 expression and cell stress response in breast cancer cells can be balanced by drug combination. Sci Rep. 2019;9(1):15099.
40. Schmid P, Rugo HS, Adams S, Schneeweiss A, Barrios CH, Iwata H, Dieras V, Henschel V, Molinero L, Chui SY, et al. Atezolizumab plus nab-paclitaxel as first-line treatment for unresectable, locally advanced or metastatic triple-negative breast cancer (IMpassion130): updated efficacy results from a randomised, double-blind, placebo-controlled, phase 3 trial. Lancet Oncol. 2020;21(1):44–59.
41. Samanta D, Park Y, Ni X, Li H, Zahnow CA, Gabrielson E, Pan F, Semenza GL. Chemotherapy induces enrichment of CD47(+)/CD73(+)/PDL1(+) immune evasive triple-negative breast cancer cells. Proc Natl Acad Sci USA. 2018;115(6):E1239–48.
42. Liu J, Zhao Z, Qiu N, Zhou Q, Wang G, Jiang H, Piao Y, Zhou Z, Tang J, Shen Y. Co-delivery of IOX1 and doxorubicin for antibody-independent cancer chemo-immunotherapy. Nat Commun. 2021;12(1):2425.
43. Yamaguchi H, Hsu JM, Yang WH, Hung MC. Mechanisms regulating PD-L1 expression in cancers and associated opportunities for novel small-molecule therapeutics. Nat Rev Clin Oncol. 2022;19(5):287–305.
44. Chow A, Perica K, Klebanoff CA, Wolchok JD. Clinical implications of T cell exhaustion for cancer immunotherapy. Nat Rev Clin Oncol. 2022;19(12):775–90.
45. Iwai Y, Ishida M, Tanaka Y, Okazaki T, Honjo T, Minato N. Involvement of PD-L1 on tumor cells in the escape from host immune system and tumor immunotherapy by PD-L1 blockade. Proc Natl Acad Sci USA. 2002;99(19):12293–7.
46. Dong H, Strome SE, Salomao DR, Tamura H, Hirano F, Flies DB, Roche PC, Lu J, Zhu G, Tamada K, et al. Tumor-associated B7–H1 promotes T-cell apoptosis: a potential mechanism of immune evasion. Nat Med. 2002;8(8):793–800.
47. Keir ME, Butte MJ, Freeman GJ, Sharpe AH. PD-1 and its ligands in tolerance and immunity. Annu Rev Immunol. 2008;26:677–704.
48. Voorwerk L, Slagter M, Horlings HM, Sikorska K, van de Vijver KK, de Maaker M, Nederlof I, Kluin RJC, Warren S, Ong S, et al. Immune induction strategies in metastatic triple-negative breast cancer to enhance the sensitivity to PD-1 blockade: the TONIC trial. Nat Med. 2019;25(6):920–8.
49. Garcia-Diaz A, Shin DS, Moreno BH, Saco J, Escuin-Ordinas H, Rodriguez GA, Zaretsky JM, Sun L, Hugo W, Wang X, et al. Interferon receptor signaling pathways regulating PD-L1 and PD-L2 expression. Cell Rep. 2017;19(6):1189–201.
50. Zhang T, Zheng S, Liu Y, Li X, Wu J, Sun Y, Liu G. DNA damage response and PD-1/PD-L1 pathway in ovarian cancer. DNA Repair (Amst). 2021;102: 103112.
51. Xu HZ, Li TF, Wang C, Ma Y, Liu Y, Zheng MY, Liu ZJ, Chen JB, Li K, Sun SK, et al. Synergy of nanodiamond-doxorubicin conjugates and PD-L1 blockade effectively turns tumor-associated macrophages against tumor cells. J Nanobiotechnol. 2021;19(1):268.

52. Bailly C. Regulation of PD-L1 expression on cancer cells with ROS-modulating drugs. Life Sci. 2020;246: 117403.
53. Sun Y, Lyu B, Yang C, He B, Zhang H, Wang X, Zhang Q, Dai W. An enzyme-responsive and transformable PD-L1 blocking peptide-photosensitizer conjugate enables efficient photothermal immunotherapy for breast cancer. Bioact Mater. 2023;22:47–59.
54. Qiu Z, Lu Z, Huang J, Zhong Y, Yan N, Kong R, Cheng H. Self-reinforced photodynamic immunostimulator to downregulate and block PD-L1 for metastatic breast cancer treatment. Biomaterials. 2023;303: 122392.
55. Krysko DV, Garg AD, Kaczmarek A, Krysko O, Agostinis P, Vandenabeele P. Immunogenic cell death and DAMPs in cancer therapy. Nat Rev Cancer. 2012;12(12):860–75.
56. Jiang M, Zeng J, Zhao L, Zhang M, Ma J, Guan X, Zhang W. Chemotherapeutic drug-induced immunogenic cell death for nanomedicine-based cancer chemo-immunotherapy. Nanoscale. 2021;13(41):17218–35.
57. Ma X, Yang S, Zhang T, Wang S, Yang Q, Xiao Y, Shi X, Xue P, Kang Y, Liu G, et al. Bioresponsive immune-booster-based prodrug nanogel for cancer immunotherapy. Acta Pharm Sin B. 2022;12(1):451–66.
58. Tang R, Xu J, Zhang B, Liu J, Liang C, Hua J, Meng Q, Yu X, Shi S. Ferroptosis, necroptosis, and pyroptosis in anticancer immunity. J Hematol Oncol. 2020;13(1):110.
59. Wang Y, Gao W, Shi X, Ding J, Liu W, He H, Wang K, Shao F. Chemotherapy drugs induce pyroptosis through caspase-3 cleavage of a gasdermin. Nature. 2017;547(7661):99–103.
60. Steinman RM. The dendritic cell system and its role in immunogenicity. Annu Rev Immunol. 1991;9:271–96.
61. Reise Sousa C. Dendritic cells in a mature age. Nat Rev Immunol. 2006;6(6):476–83.
62. Kalergis AM, Boucheron N, Doucey MA, Palmieri E, Goyarts EC, Vegh Z, Luescher IF, Nathenson SG. Efficient T cell activation requires an optimal dwell-time of interaction between the TCR and the pMHC complex. Nat Immunol. 2001;2(3):229–34.
63. Feng Q, Ma X, Cheng K, Liu G, Li Y, Yue Y, Liang J, Zhang L, Zhang T, Wang X, et al. Engineered bacterial outer membrane vesicles as controllable two-way adaptors to activate macrophage phagocytosis for improved tumor immunotherapy. Adv Mater. 2022;34(40): e2206200.
64. Chen Q, Liu L, Lu Y, Chen X, Zhang Y, Zhou W, Guo Q, Li C, Zhang Y, Zhang Y, et al. Tumor microenvironment-triggered aggregated magnetic nanoparticles for reinforced image-guided immunogenic chemotherapy. Adv Sci (Weinh). 2019;6(6):1802134.
65. Banchereau J, Briere F, Caux C, Davoust J, Lebecque S, Liu YJ, Pulendran B, Palucka K. Immunobiology of dendritic cells. Annu Rev Immunol. 2000;18:767–811.
66. Turley SJ, Inaba K, Garrett WS, Ebersold M, Unternaehrer J, Steinman RM, Mellman I. Transport of peptide-MHC class II complexes in developing dendritic cells. Science. 2000;288(5465):522–7.
67. Inaba K, Turley S, Iyoda T, Yamaide F, Shimoyama S, Reise Sousa C, Germain RN, Mellman I, Steinman RM. The formation of immunogenic major histocompatibility complex class II-peptide ligands in lysosomal compartments of dendritic cells is regulated by inflammatory stimuli. J Exp Med. 2000;191(6):927–36.
68. Ohl L, Mohaupt M, Czeloth N, Hintzen G, Kiafard Z, Zwirner J, Blankenstein T, Henning G, Förster R. CCR7 governs skin dendritic cell migration under inflammatory and steady-state conditions. Immunity. 2004;21(2):279–88.
69. Förster R, Schubel A, Breitfeld D, Kremmer E, Renner-Müller I, Wolf E, Lipp M. CCR7 coordinates the primary immune response by establishing functional microenvironments in secondary lymphoid organs. Cell. 1999;99(1):23–33.
70. Mellman I. Dendritic cells: master regulators of the immune response. Cancer Immunol Res. 2013;1(3):145–9.
71. Tanaka A, Sakaguchi S. Regulatory T cells in cancer immunotherapy. Cell Res. 2017;27(1):109–18.
72. Togashi Y, Shitara K, Nishikawa H. Regulatory T cells in cancer immunosuppression—implications for anticancer therapy. Nat Rev Clin Oncol. 2019;16(6):356–71.
73. Hui E, Cheung J, Zhu J, Su X, Taylor MJ, Wallweber HA, Sasmal DK, Huang J, Kim JM, Mellman I, Vale RD. T cell costimulatory receptor CD28 is a primary target for PD-1-mediated inhibition. Science. 2017;355(6332):1428–33.
74. Borst J, Ahrends T, Bąbała N, Melief CJM, Kastenmüller W. CD4(+) T cell help in cancer immunology and immunotherapy. Nat Rev Immunol. 2018;18(10):635–47.

Publisher's Note